Optically controlled semiconductor spin qubits for quantum information processing

2009 Phys. Scr. 2009 014010

(http://iopscience.iop.org/1402-4896/2009/T137/014010)

IOP Publishing Physica Scripta
Phys. Scr. **T137** (2009) 014010 (18pp) doi:10.1088/0031-8949/2009/T137/014010

Optically controlled semiconductor spin qubits for quantum information processing

Y Yamamoto[1,2,3], T D Ladd[1,2], D Press[1], S Clark[1], K Sanaka[1,2], C Santori[1,4], D Fattal[1,4], K M Fu[1,4], S Höfling[5], S Reitzenstein[5] and A Forchel[5]

[1] E L Ginzton Laboratory, Stanford University, 450 Via Palou, Stanford, CA 94305-4088, USA
[2] National Institute of Informatics, 2-1-2 Hitotsubashi, Chiyoda-ku, Tokyo 101-8430, Japan
[3] NTT Basic Research Laboratories, Atsugi, Kanagawa, Japan
[4] Hewlett-Packard Laboratories, 1501 Page Mill Rd, Palo Alto, CA 94304, USA
[5] Technische Physik, University of Würzburg, Am Hubland, D97074, Würzburg, Germany

Received 16 October 2009
Accepted for publication 23 October 2009
Published 14 December 2009
Online at stacks.iop.org/PhysScr/T137/014010

Abstract
Implementations of quantum information processing systems based on optically controlled electron spins in semiconductor quantum dots are particulary appealing due to several features. These features include inherent ultrafast gate operation times, reasonably long decoherence times, small optical control power and a natural ability to link to optical fiber communication networks. We will discuss the current state of the art in the experimental implementations of the main elements of semiconductor spin qubits: qubit initialization, single-qubit gates, two-qubit gates, entanglement distribution, projective measurement, quantum memory and indistinguishable single-photon generation.

PACS numbers: 03.67.−a, 42.50.Ex, 03.67.Lx, 71.35.−y, 78.67.−n

(Some figures in this article are in colour only in the electronic version.)

1. Introduction

The concepts of quantum computation and quantum simulation were first proposed by Deutsch [1] and Feynman [2], which created interest in the physical implementation of quantum information processing systems in the mid-1980s. In the late 1980s, research at NTT Basic Research Laboratories made a general search for physically implementable optical quantum information processing systems. The implementations of two qubit gates (controlled-NOT gates) and projective measurements (quantum non-demolition measurements) for flying photonic qubits based on optical Kerr nonlinearities were discussed theoretically [3, 4]. The stimulated Raman scattering process for an atomic three-level Λ-system was identified as a means of optically controlling an electronic matter qubit [3]. The experimental efforts to implement some of those ideas also started in the late 1980s. A semiconductor cavity quantum electrodynamic (QED) experiment, in which the spontaneous emission of quantum well (QW) excitons is enhanced in a monolithic planar microcavity [5, 6], was one of the outcomes of such experimental efforts. These early results from 20 years ago provided the foundation for current ideas for optically controlled semiconductor spin qubits for quantum information processing.

Since then, we have been searching for simple, practical and complete implementations of quantum information processing systems, with a special emphasis on semiconductor cavity QED and ultrafast optics techniques. Many new ingredients came into play to cope with the demanding requirements of recently discovered quantum concepts, such as fault-tolerant quantum repeaters [7, 8] and one-way quantum computation [9, 10].

The implementation of physical qubits for such future quantum information processing systems must realize the following six functions simultaneously:

(i) initialization,
(ii) single-qubit gate,
(iii) two-qubit gate,
(iv) interface to quantum communication bus and entanglement distribution,
(v) quantum memory,
(vi) projective measurement.

The last three functions (iv)–(vi) are particularly important for implementations of fault-tolerant quantum information processing systems, such as quantum repeaters based on nested purification protocols [7, 8] and fault-tolerant one-way quantum computation based on topological cluster states [9, 10]. For these applications, these abilities must be achieved with a reasonable speed and a high fidelity. Solid-state implementations based on optically controlled electron spins in semiconductor quantum dots (QDs) are particulary appealing due to their inherent ultrafast gate operation times and their natural interface to optical fiber communication networks.

The unique features of a QD as an 'artificial atom' can be summarized in the following three points:

(A) An exciton in a semiconductor QD or QW island has an enhanced oscillator strength due to an effect similar to 'Dicke's superradiance for an ensemble of atoms' [11], $f_{\text{exciton}} = f_{\text{e–h}} \times a^2/a_{\text{B}}^{*2}$, where f_{exciton} and $f_{\text{e–h}}$ are the oscillator strengths of an exciton and free electron–hole pair, a is the QD radius and a_{B}^{*} is the exciton Bohr radius. The enhancement factor a^2/a_{B}^{*2} is of the order of 10–30 for self-assembled QDs and higher for QW islands with a larger area [12–15]. This feature is the basis for ultrafast optical control of electron spins with small control powers.
(B) QDs can be placed permanently as a two-dimensional (2D) lattice at designated positions without requiring external forces [16]. The spontaneous emission rate is further enhanced by the modified field density of states with cavity walls, which provides an efficient way to couple a semiconductor spin state to an optical communication bus [17, 18]. Efficient two-qubit quantum gates, entanglement distribution and cluster state generation can also be realized optically within a monolithically integrated microcavity. A cavity mode operates as a catalyst for all those multiqubit operations.
(C) An excitonic transition wavelength can be tailored to the fiber optic communication wavelengths of 1.3–1.5 μm [19], which will facilitate a natural interface to long-distance optical communication networks.

In this paper, we will discuss how the above six functions can be potentially implemented with semiconductor QD cavity QED systems and review the current state of the art in their experimental realization.

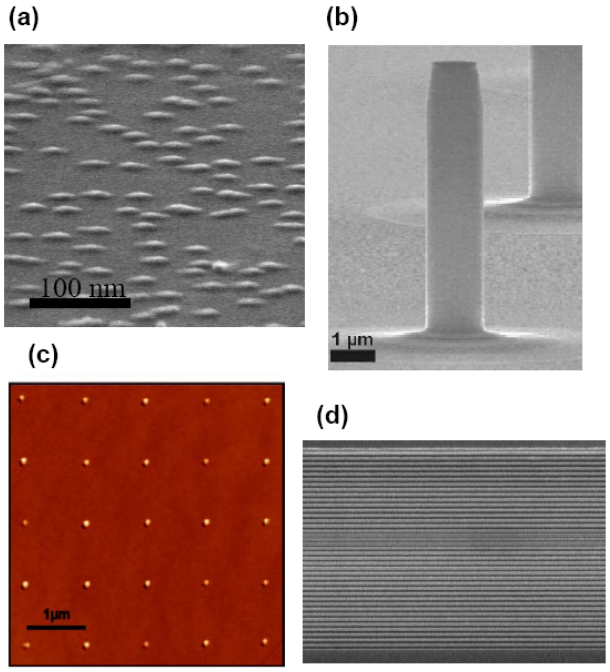

Figure 1. (a), (b) The devices used in experiments consist of self-assembled InGaAs QDs and a monolithic post-microcavity with top and bottom DBRs. (c), (d) An alternative device is based on a 2D array of position-controlled QDs and a monolithic planar microcavity with top and bottom DBRs.

2. Physical qubits—a cavity QED system with single electron-doped QDs

The device structure we most commonly use in our experiments is an ensemble of self-assembled InGaAs QDs (figure 1(a)) embedded in a 3D post-microcavity with top and bottom distributed Bragg reflectors (figure 1(b)). Because of narrow cavity resonance and large inhomogeneous broadening of QDs, a single QD coupled to a single cavity mode can be found with a reasonable probability. Alternatively, and probably preferably, a 2D array of position-controlled QDs (figure 1(c)) [16] will be embedded in a simple planar microcavity (figure 1(d)). The physical qubits in this system are the Zeeman sublevels of single electrons trapped in the QDs. These levels are split by a global dc magnetic field.

2.1. Magnetic spectrum of charged excitons in QDs

We first describe the basic optical spectroscopy of this qubit. In this experiment, a single InGaAs QD embedded in a GaAs matrix captures a single electron from a δ-doped layer of Si donor impurities located at 10–20 nm from the QD layer. A dc magnetic field B_{ext} is applied along the x-axis, perpendicular to the heterostructure growth axis and optical excitation direction (the z-axis) in this experiment (Voigt configuration). The electron Zeeman sublevels are split by $\delta_{\text{e}} = \mu_{\text{B}} g_{\text{e}} B_{\text{ext}}$ in frequency, where μ_{B} is the Bohr magneton and g_{e} is the electron gyromagnetic ratio, which may be drastically different from that of a bare electron (2.0013). This ratio is about -0.35 for our system due to the relatively strong spin–orbit coupling. The excited state with an additional

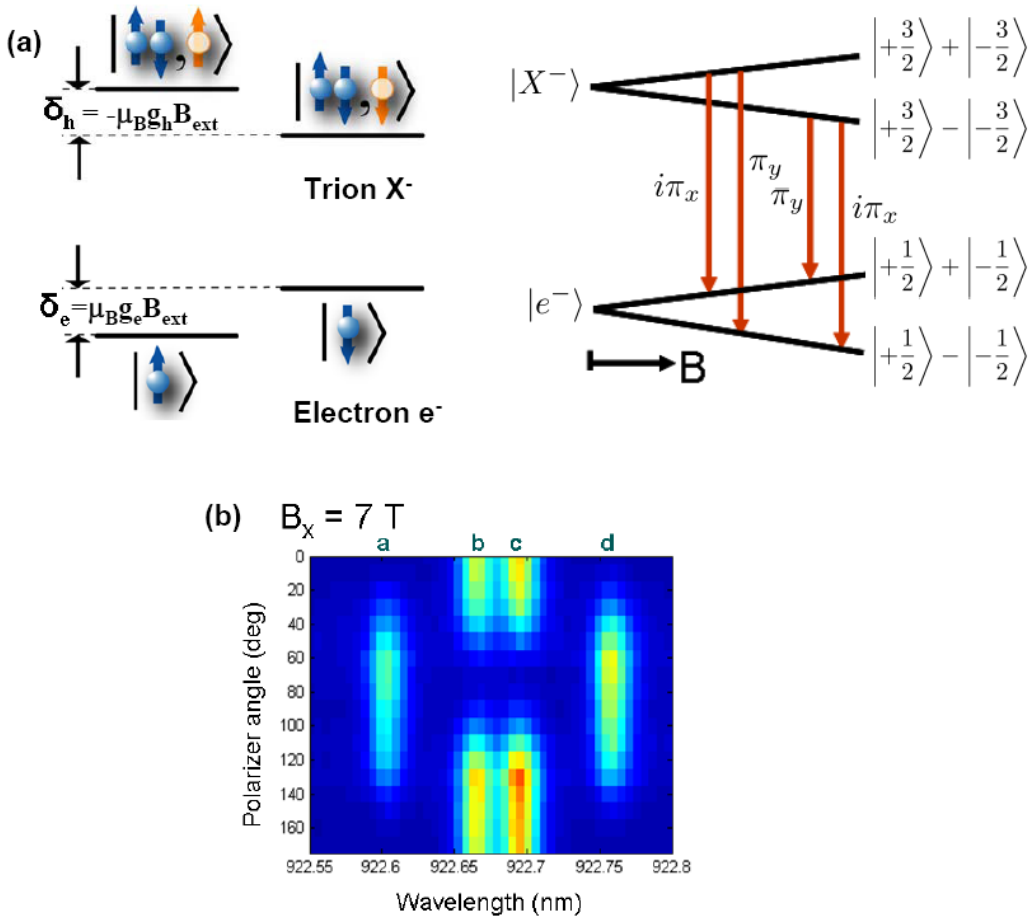

Figure 2. (a) The energy splitting of an electron spin and trion state in an InGaAs QD under Voigt configuration as well as the polarization selection rules. (b) The observed magnetic spectrum and polarization direction of the excitonic emission [21].

electron–hole pair is called a charged-exciton or trion state. For this state, the two electrons are in a spin singlet state, and so an unpaired hole determines the spin. Hole states are split due to a variety of effects. The relatively large energy splitting between the heavy hole ($m_z = \pm 3/2$) and light hole ($m_z = \pm 1/2$) due to the strong confinement along the z-axis allows us to neglect the light–hole contribution to the magnetic spectrum. We neglect the electron–hole exchange interaction, as it is small compared with the Zeeman energy at $B_{\text{ext}} = 5$–$10\,T$ [20]. If we represent the trion state splitting at our magnetic field as an effective Zeeman splitting, $\delta_{\text{h}} = \mu_{\text{B}} g_{\text{h}} B_{\text{ext}}$, then the effective hole gyromagnetic ratio g_{h} is approximately -0.30. The energy spectrum of such a two-fold three-level Λ system is schematically shown in figure 2(a), as well as the polarization selection rules for the four transition lines. These features have been fully confirmed experimentally as shown in figure 2(b) [21].

The excitonic emissions at the highest and lowest transition energies are linearly polarized along the y-axis, while the emissions at two inner transition lines are linearly polarized along the x-axis. There is a $\frac{\pi}{2}$ phase difference between the two transitions. In a subsequent single-pulse-stimulated Raman scattering experiment [21], we used a circularly polarized pump pulse, for which the two stimulated Raman scattering amplitudes via two trion states constructively interfere.

2.2. *Enhanced spontaneous emission rate for a QD exciton*

The existence of a single isolated QD can be conveniently confirmed by the excitonic emission featuring a strong anti-bunching effect ($g^{(2)}(0) \leqslant 1/2$) as shown in figure 3(a) [22]. In this particular InGaAs QD system, the spontaneous emission lifetime of the QD in a homogeneous GaAs matrix is ∼620 ps, while it is reduced to ∼15 ps in a post-microcavity with a post-diameter of 1.8 μm (figure 1(b)). Therefore, a spontaneous-emission-rate enhancement factor, often referred to as Purcell factor or cooperativity parameter, is $F_{\text{P}} \equiv \gamma/\gamma_0 - 1 \sim 60$, where γ and γ_0 are the spontaneous emission rates inside and outside a cavity, respectively. In the experimental result shown in figure 3(b), the enhanced spontaneous emission rate is roughly equal to the cavity decay rate, so that the system is slightly inside the strong coupling regime. This regime results from a relatively small cavity mode volume $V_0 \sim 20(\lambda/n)^3$ and large cavity Q value ($\sim 1.5 \times 10^4$) [22]. We emphasize that a strong coupling is not essential to implement various quantum information processing elements described in this paper.

However, a large Purcell factor is indispensable for implementing efficient two-qubit gates and entanglement distribution protocols. For an atomic point dipole in a planar microcavity, such a large Purcell factor is achieved only if the top and bottom DBRs are formed with two materials with large refractive-index difference [23]. This is because the isotropic radiation pattern of a point dipole is poorly matched

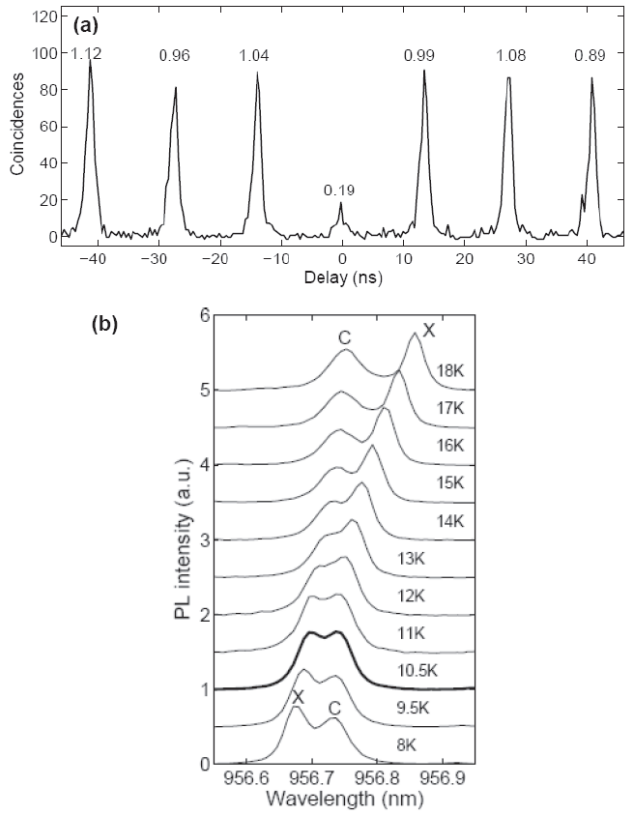

Figure 3. (a) A measured two photon correlation trace $g^{(2)}(\tau)$ for the excitonic emission from a single QD in a post-microcavity. (b) The photoluminescence spectra from this system for various exciton-cavity detuning parameters where the excitonic transition wavelength is swept by a temperature [22].

to the narrow radiation pattern along the normal direction of a high-Q planar microcavity. The increased refractive-index difference helps to increase the acceptance angle of the DBR so that more efficient enhancement of spontaneous emission rate becomes possible.

In the case of a QD with a finite lateral size, the radiation pattern is concentrated onto a normal direction even in a homogeneous medium when ka approaches to one, where $k = 2\pi n/\lambda$ is the optical wavenumber and a is the QD diameter. For an InGaAs QD emitting at 900 nm, the above condition corresponds to $a \geqslant 40$ nm, which is easily achieved by self-assembled QDs. The spontaneous emission rate is also enhanced due to the superadiance effect [12]. However, the enhanced oscillator strength $f_{\text{exciton}} = f_{\text{e–h}} \times a^2/a_{\text{B}}^{*2}$ is off-set by the reduced density of field states when $ka \gg 1$, and the enhanced spontaneous emission rate saturates at $\tau_0/\tau \sim 6/\pi^2(\lambda/na_{\text{B}}^*)^2$, where τ and τ_0 are the spontaneous emission lifetimes for an exciton and a free electron–hole pair. The numerically evaluated spontaneous emission rate enhancement factor approaches the saturation value $\tau_0/\tau \sim 350$ when ka exceeds one [12]. A spontaneous emission lifetime of 20–100 ps was indeed observed in large area QDs [13–15], while a spontaneous emission lifetime of an electron–hole pair is of the order of 5–10 ns. Since the inherent radiation pattern of a large area QD naturally matches the radiation pattern of a high-Q planar microcavity, an even larger Purcell factor can be expected for such a system. Figure 4 shows the calculated spontaneous emission

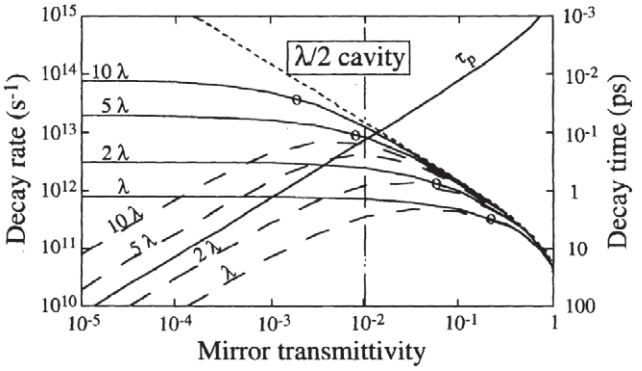

Figure 4. The spontaneous emission lifetime versus DBR mirror transmittivity for a half-wavelength planar cavity for various system size a. The cavity photon lifetime τ_{p} is also plotted. The dotted line is the asymptotic decay rate, $\frac{1}{\tau} \sim \frac{6}{\pi^2}(\frac{\lambda}{na_B^*})^2 \frac{1+\sqrt{R}}{1-\sqrt{R}} \frac{1}{\tau_0}$. The dashed lines correspond to the decay time of an inhomogeneously broadened exciton transition line with a 5 meV linewidth [12].

decay rate of a QD exciton in a half-wavelength planar microcavity versus DBR transmittivity (1-R) for various QD radii [12]. Compared to the spontaneous emission lifetime of 5–10 ns for a free electron–hole pair, the lifetime is decreased to ∼20 ps for a QD exciton without a cavity, and it is further decreased to ∼1 ps with a cavity when $a \simeq \lambda/n$. The spontaneous emission lifetime of ∼1 ps was observed for a single QW exciton in a GaAs/AlAs planar microcavity [24]. This particular transition matches very well to a high-Q planar microcavity, which is a main motivation to use a semiconductor QD or QW island as an 'artificial atom'.

3. Qubit initialization by optical pumping

A basic scheme for initializing an electron spin in its ground state $|0\rangle$ via optical pumping is shown in figure 5(a), where the transition between the states $|1\rangle$ and $|e\rangle$ is selectively pumped and the trion state decays into the state $|0\rangle$ after a few transition cycles. Figure 5(b) shows the measured population in the state $|1\rangle$ for the repeated process of optical pumping over 13 ns and ultrafast π-pulse rotation (electron spin flip) [21]. This spin-flip process will be discussed in the following section. From this result, the initialization fidelity by optical pumping over 13 ns is estimated to be $92 \pm 7\%$. If a standard thermal equilibration technique was used for qubit initialization, we would need a high magnetic field and low temperature for satisfying $\delta_{\text{e}} = \mu_{\text{B}} g_{\text{e}} B_{\text{ext}} \gg k_{\text{B}} T$; further we would need to wait for the relatively long spin equilibration time, which is $T_1 \gtrsim 1$ ms in our system.

A potentially more efficient and faster way to initialize an electron spin is to use a (single shot) projective measurement of the electron spin state. If the measurement result is $|0\rangle$, the initialization is complete; if the measurement result is $|1\rangle$, we can send a π-pulse to flip the electron spin state. We will discuss such a projective measurement of an electron spin in section 6.

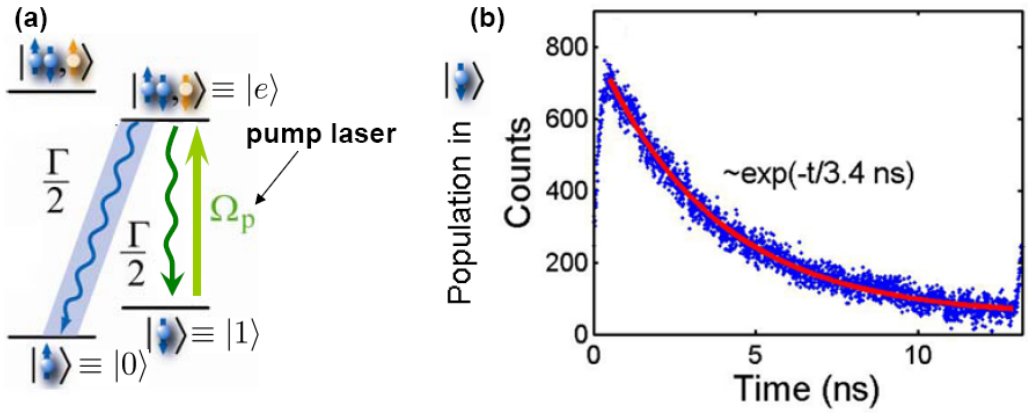

Figure 5. (a) Optical pumping scheme to initialize the electron spin in its ground state $|0\rangle$. (b) The measured population in the electron spin excited state for a repeated process of optical pumping and π-pulse spin rotation [21].

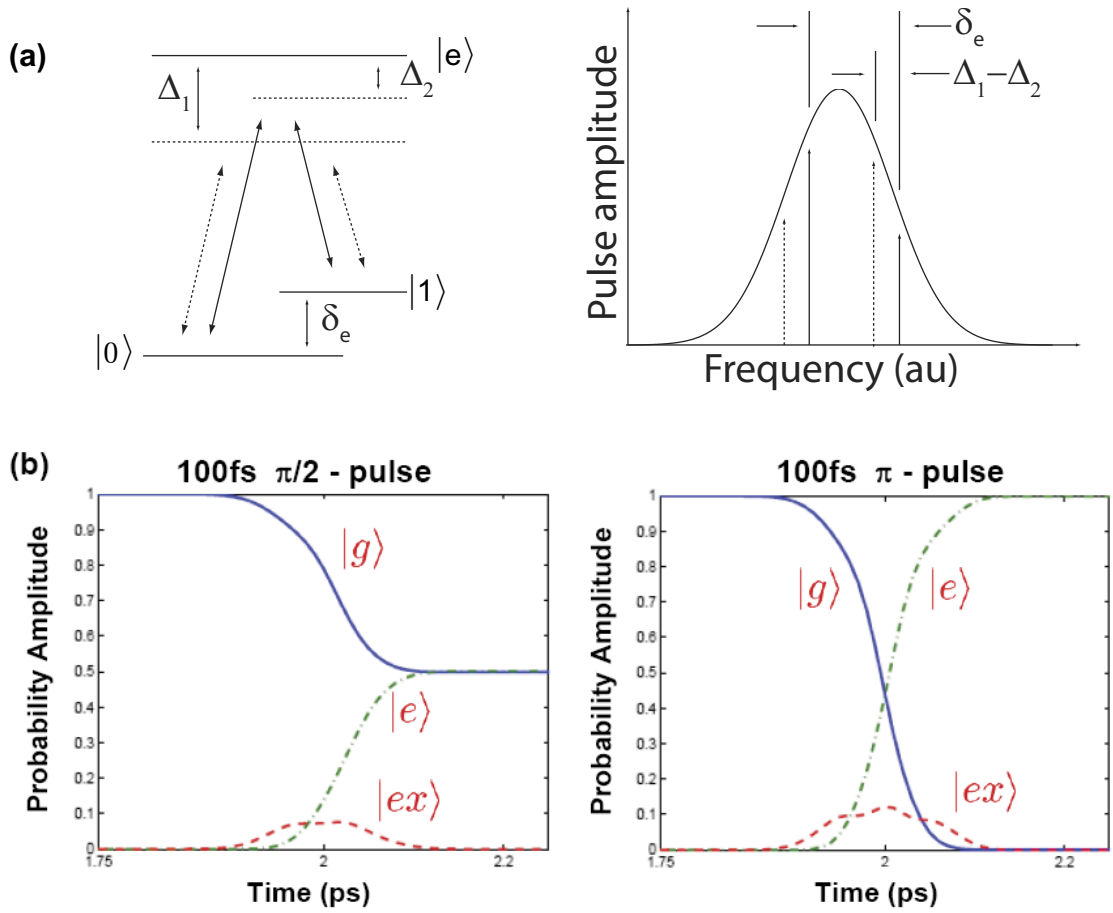

Figure 6. (a) The energy level diagram of a charged QD and two pairs of frequencies contained in the pulse spectrum that will induce transitions between $|0\rangle$ and $|1\rangle$. (b) Probabilities for the states $|0\rangle$, $|1\rangle$ and $|e\rangle$ for a $\frac{\pi}{2}$ and π-pulse excitation [25].

4. One-qubit gate by single, broadband, stimulated-Raman-scattering pulses

A single short optical pulse with a broad spectrum can implement an arbitrary one qubit gate for these qubits [25]. As shown in figure 6(a), an electron-doped QD may automatically find an upper and lower sideband from the pulse spectrum; these frequency bands connect the two spin states $|0\rangle$ and $|1\rangle$ by off-resonant-stimulated Raman scattering, for a variety of possible detuning values Δ. A continuum of such pairs of upper and lower sidebands exist in the spectrum of a broadband pulse. If the phase differences between the two sidebands are identical for all pairs, constructive interference occurs among the continuum of distributed-Raman-scattering paths, leading to highly efficient electron spin rotation. The condition of the constant phase difference between the upper and lower sidebands is satisfied if the optical pulse is Fourier-transform limited. This spin rotation may alternatively

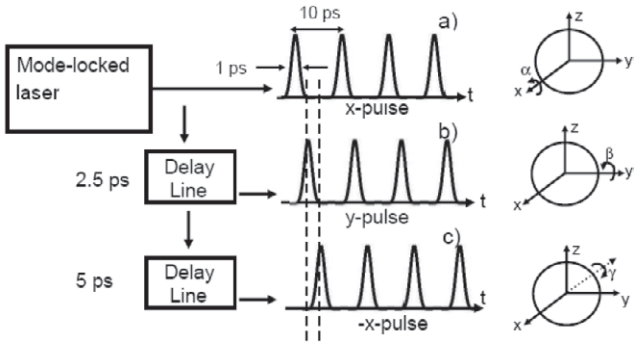

Figure 7. Rotations of an electron spin about various axes induced by optical pulse delays. (a) x-pulse, (b) y-pulse, and (c) $-x$-pulse [25].

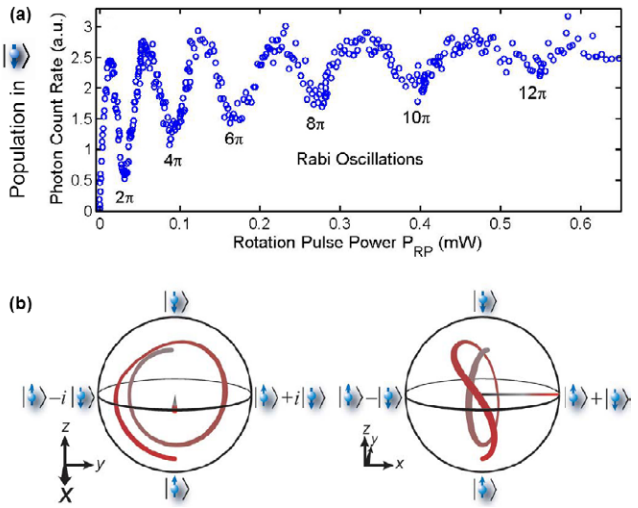

Figure 8. (a) Coherent Rabi oscillations between the electron spin states versus optical pulse power. (b) Evolution of the reconstructed Bloch vector over the range of rotation angles $0 \leqslant \theta \leqslant 3\pi$. Views are from the x-axis and $-y$-axis, respectively. The rotation angle and Bloch vector length are extracted from the extreme of the coherent Rabi oscillation data (figure 8(a)) and the azimuthal position of the Bloch vector is determined from the phase of the Ramsey fringes (figure 9) [21].

be interpreted as an optical Stark shift [26] of the optically bright superposition of $|0\rangle$ and $|1\rangle$ with respect to an optically dark superposition.

If the electron Zeeman frequency δ_e, the detuning $\Delta_0(\Delta_1)$ of the pulse center frequency from the $|0\rangle \leftrightarrow |e\rangle(|1\rangle \leftrightarrow |e\rangle)$ excitonic transition frequency and the coherent Rabi frequencies $\Omega_0(t), \Omega_1(t)$ due to the pulse satisfy $\delta_e \ll \{\Omega_0, \Omega_1\} \ll \{\Delta_0, \Delta_1\}$, then the time-dependent effective Rabi frequency between the two qubit states $|0\rangle$ and $|1\rangle$ is approximately given by

$$\Omega_{\text{eff}}(t) \simeq \frac{\Omega_0(t)\Omega_1^*(t)}{2\Delta} \simeq \frac{|\Omega(t)|^2}{2\Delta}, \tag{1}$$

where Δ is the average of Δ_0 and Δ_1. A circularly polarized pulse ensures that the probability amplitudes from the two Λ systems add constructively, and a large detuning Δ minimizes undesired real excitation in the excited states $|e\rangle$.

Figure 6(b) shows the numerical simulation results based on a three-level master equation for an ultrafast $\pi/2$-pulse and π-pulse [25]. The state $|e\rangle$ is only virtually populated during the pulse excitation and the high fidelity of 99.9% can be achieved with single optical pulses with a duration of 100 fs in spite of reasonable decoherence time for the $|e\rangle$ state (electron spin decoherence time $T_2 = 10\,\mu$s; exciton spontaneous lifetime $\tau_0 = 200$ ps, Zeeman frequency $\delta_e/2\pi = 100$ GHz). This result indicates that a huge transverse magnetic field ($B_{\text{optical}} \sim 10^3$ T) can be effectively induced by optical pulses for a duration of 100 fs. The required pulse energies are 5 μJ cm^{-2} and 14 μJ cm^{-2} for $\pi/2$ and π-pulses, respectively, which are easily available from a mode-locked semiconductor laser system.

A system clock signal is provided by the repetition frequency of a mode-locked laser as shown in figure 7 [25]. An electron Larmor frequency δ_e can be locked to the repetition frequency of the mode-locked laser, which provides a clock signal to the whole system. The optical pulse arriving at $t = 0$ has zero phase difference between the upper and lower sidebands shown in figure 6(a) such that it rotates the electron spin about the x-axis. The optical pulse arriving a quarter Larmor period later $t = \pi/2\delta_e$ has a $\pi/2$ phase difference between the upper and lower sidebands so that it rotates the electron spin about the y-axis. Similarly, the optical pulse arriving a half Larmor-period later $t = \pi/\delta_e$ rotates the electron spin about the $-x$-axis. Since an arbitrary one qubit gate (i.e. an SU(2) operation on a qubit) can be decomposed into the three rotation operators, $\hat{R}_x(\alpha)\hat{R}_y(\beta)\hat{R}_{-x}(\gamma)$, the three optical pulses at $t = 0, \pi/2\delta_e$ and π/δ_e can implement an arbitrary SU(2) operation. The time required for an arbitrary gate is therefore as short as $\sim$10 ps for $\delta_e/2\pi \sim 50$ GHz.

Figure 8(a) shows the experimentally induced coherent Rabi oscillation by a single optical pulse of 4 ps pulse duration with $\delta_e = 26$ GHz and $\Delta = 270$ GHz [21]. The electron spin is rotated with angles up to 12π as the pulse power is increased. Figure 8(b) shows the trajectory of a reconstructed electron spin state in a Bloch sphere seen from the x-axis (along a rotation axis) and from the y-axis (orthogonal to the rotation axis) up to the pulse area of 3π.

Incomplete initialization ($F_{\text{initial}} \sim 92\%$) degrades the purity of an initial state in this experiment, which is seen as the reduced length of a Bloch vector pointing to the south pole at $t = 0$ in figure 8(b). After a $\pi/2$ rotation, the purity is further decreased due to the decoherence induced by the incoherent absorption of the optical pulse. This unwanted background absorption is likely due to the weak absorption tail of a QW (wetting layer), and might be eliminated by growing QDs without a wetting layer. After a π rotation, the electron spin direction is skewed from the north pole direction due to the non-negligible Larmor precession (with a period of $\sim$40 ps) of the electron spin during the 4 ps pulse excitation. This problem can be overcome by using shorter optical pulses and lower dc magnetic field.

The Ramsey interferometer for an electron spin is constructed with two optical pulses and variable delay time. The interference pattern is shown in figure 9 for various pulse areas and delay times. To estimate the fidelity of the $\pi/2$ pulses, we assume the Bloch vector initially has normalized length of $L_0 = 0.83$ (determined from the initial fidelity of 92%) and directed toward the south pole of the Bloch

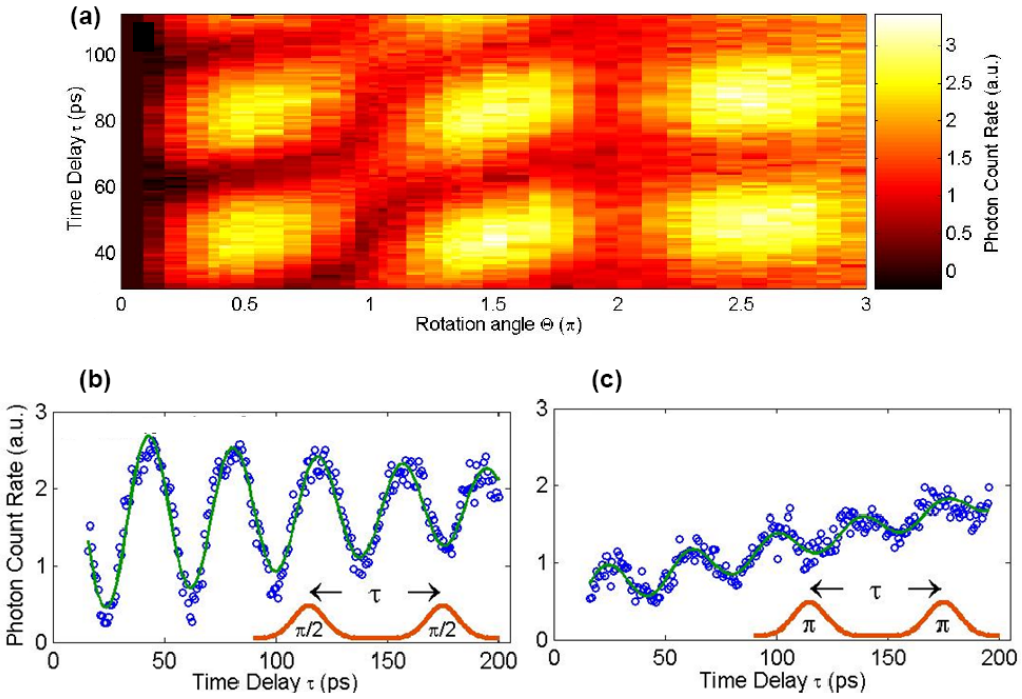

Figure 9. Experimental demonstration of Ramsey fringes. (a) Photon count rate is color mapped as a function of pulse rotation angle θ and delay time between pulses. (b) Ramsey fringes for a pair of $\pi/2$ pulses. (c) Ramsey fringes for a pair of π-pulses [21].

sphere. It shrinks in length by a factor of $D_{\pi/2}$ due to a $\pi/2$ pulse. The Bloch vector length after two $\pi/2$ pulses is thus $L_0 D_{\pi/2}^2$, and thus the population in state $|1\rangle$ oscillates between $(1+L_0 D_{\pi/2}^2)/2$ and $(1-L_0 D_{\pi/2}^2)/2$ with a Larmor period of $2\pi/\delta_e$. The fidelity is defined by $F_{\pi/2} = (1+D_{\pi/2})/2$. We estimate the fidelity by considering the Ramsey fringe amplitude at the shortest delay time (figure 9) as $F_{\pi/2} \sim 0.94$ [21].

Ideally, the Ramsey interferometer output would remain constant at $L_0(1-D_\pi^2)/2$ with no oscillations for a π-pulse case. However, the experimental result shows an overall upward slope, due to the optical pumping beam remaining on between two π-pulses and pumping population from $|1\rangle$ state to $|e\rangle$ state. Small oscillations remain because the rotation axis is not exactly the x-axis, as discussed earlier. The π-pulse rotates the spin about a vector titled by 0.17 rad from the x-axis, as shown in figure 8(b). By comparing the length and orientation of the Bloch vector with a vector with the same length as the initial state but in the direction of the north pole, we estimate the fidelity to be $F_\pi \sim 0.91$ [21].

5. Two-qubit gate by single narrow band pulses

Implementation of a two-qubit gate is often realized by using some kind of quantum communication bus, which connects two qubits. Examples include a phonon bus for trapped ions and a cavity/waveguide photon bus for semiconductor QDs and Josephson junctions. In contrast to the methods using a direct exchange interaction or dipole coupling between spins, the use of a quantum communication bus provides more freedom to design a quantum circuit and often allows non-local gate operation between two distant qubits. However, in most cases, the qubit-bus entanglement will also become a source of decoherence. This is a particulary serious problem for an optical quantum communication bus in which photon loss is unavoidable.

A deterministic two-qubit gate may be implemented by a common cavity mode including two qubits. The gate is achieved by driving the cavity mode with one or more optical pulses from a laser. The phase or amplitude of this cavity mode may be altered by the state of the qubits, which in turn changes the phase or population of those qubits. The amplitude version of such a gate was proposed in [27], and may be viewed as a pair of stimulated Raman transitions for two qubits driven by two lasers and their common cavity mode [3]. This gate is known to require high-Q cavities and may present problems for scaling up toward a large system. The phase version of such a gate is a form of the 'qubus' gate described in [28], and may be viewed as a geometric (or Berry's) phase gate in which two qubits and a photonic waveguide mode are entangled and then disentangled after the entire interaction, so that the waveguide mode can be discarded without measurement. This gate is known to be sensitive to internal photon loss [17, 18, 25].

One of the simplest two-qubit gates of the phase version is shown in figure 10(a) [29]. We assume that the 2D array of position-controlled QDs is embedded at the center of a common planar microcavity. A narrow band optical pulse with a matched spot size to the inherent mode size of a planar microcavity and a center frequency slightly detuned from the $|1\rangle \rightarrow |e\rangle$ transition is incident upon a spot where the two particular QDs (qubits) exist. The inherent mode size of a planar microcavity is determined by the cavity Q value and ranges from 1 to 100 μ [12]. The advantage of using a planar microcavity is the flexibility and simplicity that an independent cavity with a unique mode area determined by the cavity Q value can be formed at any desired position inside a whole wafer.

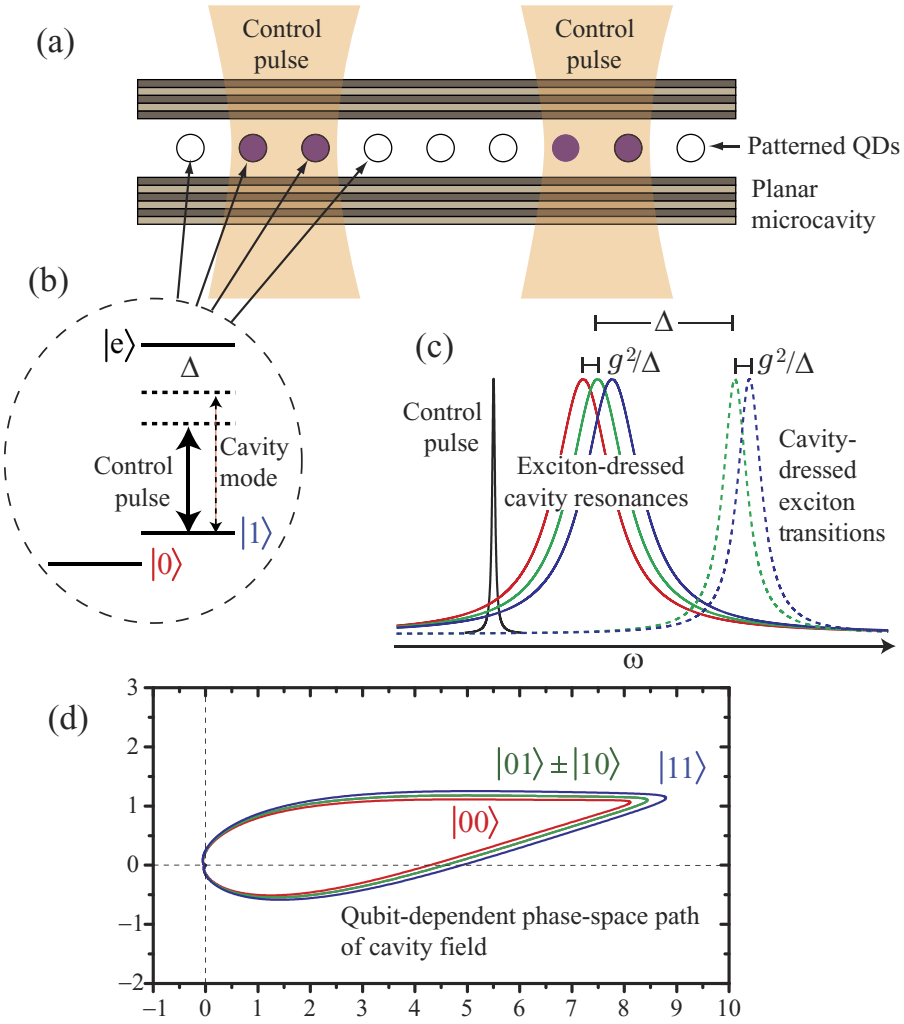

Figure 10. (a) 2D array of position-controlled QDs in a planar microcavity for which a two-qubit gate is implemented at any position by sending a coherent state pulse. (b) Example level structure assumed for a single QD; for simplicity, we consider that only state $|1\rangle$ is optically connected to the exciton state $|e\rangle$. (c) Qubit-dependent cavity resonance and control-pulse spectrum. The cavity dresses the excitonic transitions; the excitonic transitions dress the cavity. The effective detuning of the control field is determined by the atomic state, color coded with red representing $|00\rangle$, green representing superpositions of $|01\rangle$ and $|10\rangle$, and blue representing $|11\rangle$. (d) Phase-space trajectory of the cavity internal field for qubit states $|00\rangle$, $|01\rangle$ or $|10\rangle$ and $|11\rangle$, respectively [29].

Next, we will explain how this two-qubit gate works. Since the empty cavity resonance is close the $|1\rangle \rightarrow |e\rangle$ excitonic transition line, the cavity resonance frequency depends on the spin state of the two QDs as shown in figure 10(c). For a given incident pulse power with a detuning center frequency from the cavity resonance as shown in figure 10(b), the cavity internal field amplitude depends on the cavity resonance frequency, i.e. the two-qubit states. Figure 10(d) shows the qubit-state-dependent phase-space trajectory of the cavity internal field, simulated by a master equation with two $|1\rangle \rightarrow |e\rangle$ excitonic transitions and coherent state input field. As a Gaussian pulse enters and exits the cavity, a trajectory is swept out; however, the exact shape depends on the qubit-induced cavity detuning. When the difference in the enclosed areas of these phase-space trajectories becomes π, a universal two-qubit gate, identical to a controlled-phase gate up to single-qubit rotations, can be implemented [17, 18, 28]. An alternative but equivalent explanation of this two-qubit gate is the following: depending on the qubit state 1, the cavity resonance and therefore its internal field amplitude is modulated. Qubit 2 is subject to the ac Stark shift from this modulated field. In this way, one qubit controls the other's phase, mediated by the cavity.

In order to achieve a high fidelity for this two-qubit gate, we have to consider two decoherence mechanisms. One is the spontaneous emission due to real absorption of incident control pulse photons and real excitation to the excited $|e\rangle$ state. To minimize this, detuning of the pulse center frequency from the $|1\rangle - |e\rangle$ exciton transition should be sufficiently large and the incident control pulse power should not be too strong. The other decoherence mechanism is the loss of photons through a cavity mirror, which reveals 'which-path' information. As shown in figure 10(d), the qubit and the cavity internal field may be continuously entangled during the entire pulse duration. In other words, the photon field is phase modulated by the dispersive coupling with the qubit states. The difference in the amplitude and phase of the cavity internal field should be overwhelmed and hidden by the quantum noise (vacuum fluctuations). We must realize a so-called quantum erasure process by utilizing the

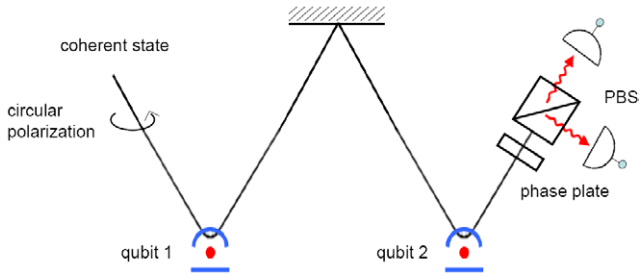

Figure 11. An entanglement distribution scheme based on a coherent-state bus. A polarization interferometer is assumed here instead of a Mach–Zehnder interferometer of van Loock *et al* [17, 18].

intrinsic quantum noise of a weak coherent state. For this reason, the detuning of the pulse center frequency from the $|1\rangle \rightarrow |e\rangle$ transition must be limited. Optimization of the gate is therefore a trade-off between the two decoherence mechanisms.

Through a numerical search for an optimized parameter range, we find the gate fidelity of approximately 95% can be achieved with a cavity Q value of 10^5, and cavity detuning of 100 GHz with optical control pulse duration in the nanosecond regime. Higher fidelity requires cavities with a higher ratio of Q to mode volume, or more sophisticated methods for quantum erasure.

6. Entanglement distribution and projective measurement

Distant two-qubit gate and qubit-transfer operations require the preparation of an entangled state in remote quantum memories and the use of quantum teleportation. Entanglement distribution between two remote quantum memories can be achieved either with a coherent state bus [17, 18] or single-photon bus [30–32]. The qubit-coherent-state-bus entanglement also provides an efficient means of projective measurements of a single qubit.

6.1. A coherent-state bus

A basic scheme of entanglement distribution with a coherent state bus is shown in figure 11 [17, 18]. A circularly polarized coherent state pulse is incident upon one spot in a planar microcavity where a qubit 1 is prepared in a linear superposition state, $\frac{1}{\sqrt{2}}(|0\rangle + |1\rangle)_1$. Through the polarization-selective dispersive coupling, the qubit state and field polarization state are entangled into the state $\frac{1}{\sqrt{2}}(|0\rangle_1|\frac{\pi}{2}\rangle_f + |1\rangle_1|\frac{\pi}{2}+\theta\rangle_f)$, where $|\frac{\pi}{2}\rangle_f$ and $|\frac{\pi}{2}+\theta\rangle_f$ correspond to the phase difference of the two (x and y) linear polarization components. If we repeat an exactly same process for the other spot where qubit 2 is also prepared in $\frac{1}{\sqrt{2}}(|0\rangle + |1\rangle)_2$, the final state of the combined qubits and field is $\frac{1}{2}[|0\rangle_1|0\rangle_2|\frac{\pi}{2}\rangle_f + (|0\rangle_1|1\rangle_2 + |1\rangle_1|0\rangle_2)|\frac{\pi}{2}+\theta\rangle_f + |1\rangle_1|1\rangle_2|\frac{\pi}{2}+2\theta\rangle_f]$.

We can easily measure a phase difference between the two polarization components and if $|\frac{\pi}{2}+\theta\rangle_f$ is post-selected, the two-qubit state is projected onto the entangled state $\frac{1}{\sqrt{2}}(|0\rangle_1|1\rangle_2 + |1\rangle_1|0\rangle_2)$ with a success probability of 50%.

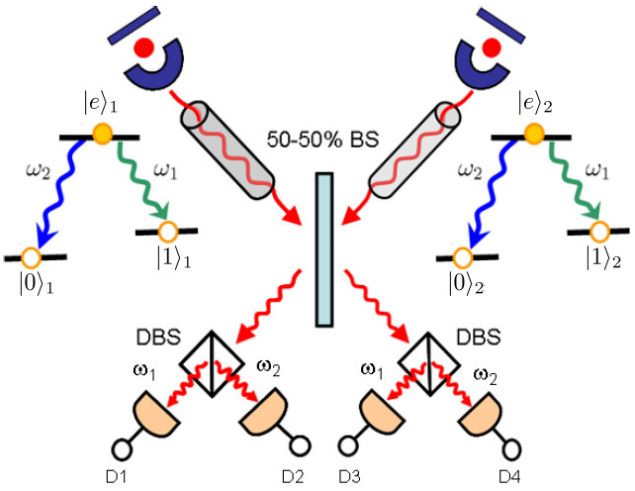

Figure 12. An entanglement distribution scheme based on a single photon bus. BS: beam splitter, DBS: dichroic beam splitter.

The advantage of this scheme is a fast operation time, high success probability and robustness against optical path (phase) fluctuation due to the employed polarization interferometry configuration. The disadvantage is the fidelity degradation due to photon loss between the two interactions, because dangerous entanglement exists between the qubit 1 and the field polarization during that interval. Indeed, this entanglement can be exploited for a means of single shot projective measurement of qubit 1.

6.2. A single photon bus

A basic scheme of entanglement distribution with a single photon bus is shown in figure 12. Two QDs are simultaneously excited to the charged exciton states $|e\rangle_1$ and $|e\rangle_2$. Through a spontaneous emission process, both QDs emit photons either at ω_1 or ω_2 to reach a qubit state $|1\rangle$ or $|0\rangle$, respectively. Therefore, we have two pairs of qubit-field entangled states: $\frac{1}{\sqrt{2}}(|0\rangle_1|\omega_2\rangle_{f_1} + |1\rangle_1|\omega_1\rangle_{f_1})$ and $\frac{1}{\sqrt{2}}(|0\rangle_2|\omega_2\rangle_{f_2} + |1\rangle_2|\omega_1\rangle_{f_2})$. If the two field modes f_1 and f_2 are occupied by pairwise quantum mechanically indistinguishable single photons and are recombined at a 50–50% beam splitter, the output state is

$$\begin{aligned}&\tfrac{1}{4}\,(|1\rangle_1|0\rangle_2 + |0\rangle_1|1\rangle_2) \otimes \left(|\omega_1\rangle_{f_2}|\omega_2\rangle_{f_2} - |\omega_1\rangle_{f_1}|\omega_2\rangle_{f_1}\right)\\ &+ \tfrac{1}{4}\,(|1\rangle_1|0\rangle_2 - |0\rangle_1|1\rangle_2) \otimes \left(|\omega_1\rangle_{f_2}|\omega_2\rangle_{f_1} - |\omega_1\rangle_{f_1}|\omega_2\rangle_{f_2}\right)\\ &+ \text{other terms.}\end{aligned} \tag{2}$$

Therefore, if the detectors D1 and D2 simultaneously click or the detectors D3 and D4 simultaneously click, the two-qubit states are projected onto the entangled state, $\frac{1}{\sqrt{2}}(|1\rangle_1|0\rangle_2 + |1\rangle_1|0\rangle_2)$. On the other hand, if the detectors D1 and D4 simultaneously click or the detectors D2 and D3 simultaneously click, the two-qubit states are projected onto the entangled states, $\frac{1}{\sqrt{2}}(|1\rangle_1|0\rangle_2 - |0\rangle_1|1\rangle_2)$.

The advantage of this scheme is that the fidelity of the resulting entanglement is robust against photon loss. Since the Zeeman frequency $\omega_2 - \omega_1$ is $\sim 10^{-4}$ of the optical carrier frequencies ω_1, ω_2, the optical path (phase) fluctuation can be suppressed by the same factor ($\sim 10^{-4}$) [30–32]. The disadvantage is the low success probability, since a single

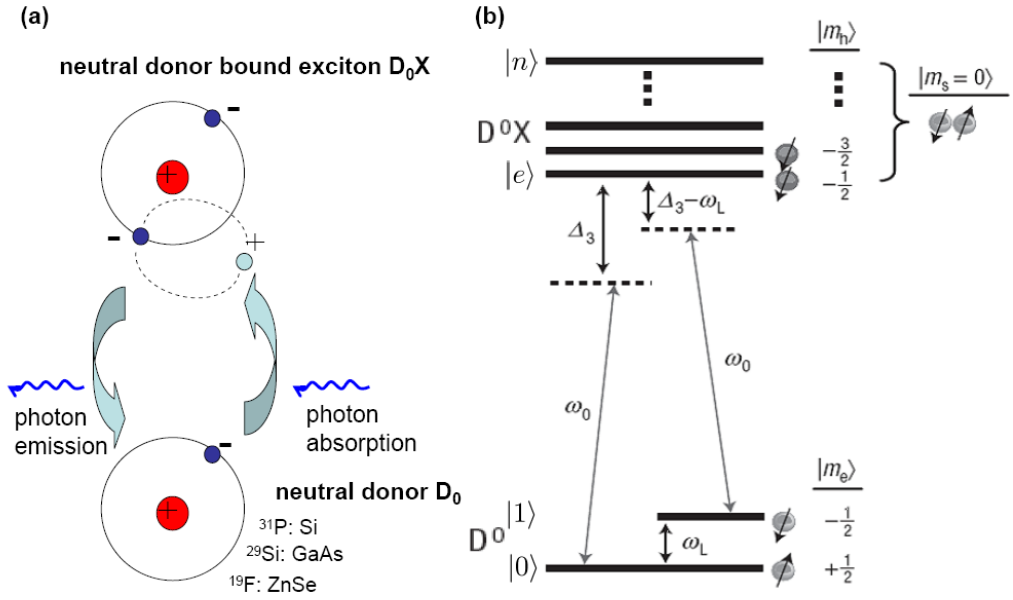

Figure 13. (a) A neutral donor D_0 and donor bound exciton D_0X in semiconductors. (b) Energy levels of D_0 and D_0X states in a dc magnetic field.

photon can be easily lost due to scattering, absorption and reflection loss of optical circuits, and we require a coincidence count. Entanglement has been formed recently in two trapped ions based on this scheme [33].

7. Quantum memory

In a quantum repeater system with an ultralong communication distance of 1000–10 000 km, qubits must be stored for an extremely long time up to 1–10 s [7, 8], while quantum gate operations are performed very rarely for qubits. In such systems, repeated quantum error corrections for qubits stored in electron spin quantum processors are not convenient. Instead, we can think of the use of a long-lived quantum memory to store qubits. A substitutional donor impurity in semiconductors is a 'natural QD', which possesses such a quantum memory function.

7.1. Magnetic spectrum of donor bound excitons

Figure 13(a) shows the ground state and excited state of neutral donor impurities such as ^{31}P:Si, ^{29}Si:GaAs and ^{19}F:ZnSe. These donor impurities have a simplest nuclear spin $-1/2$ and capture an unpaired electron at low temperatures. The contact hyperfine coupling between a single electron spin and nuclear spin is ∼60, 10 and 100 KHz for ^{31}P:Si, ^{19}F:ZnSe and ^{29}Si:GaAs, respectively. These neutral donor impurities D_0 can capture an electron–hole pair (bound exciton), which is the excited state and provides various optical capabilities to these systems via resonant photon absorption, spontaneous emission, off-resonant dispersive interactions and stimulated Raman transitions.

Two electrons in a neutral donor bound exciton D_0X are in a spin singlet state, so the spin state of the bound exciton is determined by an unpaired hole. Figure 13(b) shows the energy levels of D_0 and D_0X of a ^{29}Si:GaAs system under a dc magnetic field [34]. The magnetic

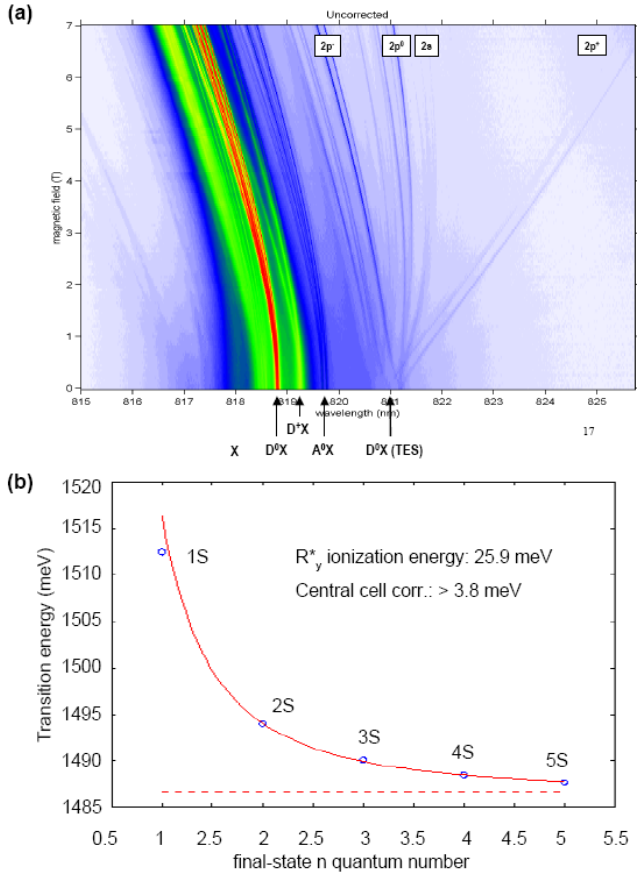

Figure 14. (a) The magnetic spectrum of Si:GaAs donor bound excitons. (b) The transition energies of the two hole satellite emissions from acceptor bound excitons in GaAs. The dashed line represents the transition energy to the ionization threshold, $E_{A_0X} - E_{A_0}$.

spectrum for the D_0X–D_0 transition of an ensemble of Si:GaAs under non-resonant above band excitation is shown in figure 14(a) [35]. The blue shift of a D_0X line is due to a

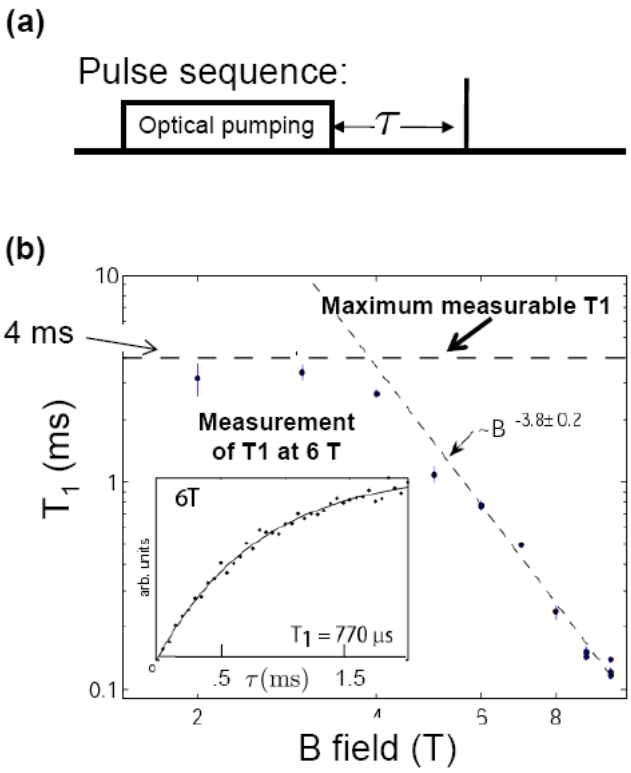

Figure 15. (a) A pulse sequence for measuring the spin relaxation time T_1 time for a Si:GaAs system. (b) The measured T_1 versus dc magnetic field B_{ext}. Inset: population in the excited spin state after switching off an optical pumping beam.

diamagnetic shift (reduction of an exciton wavefunction due to the applied field). The D_0X lines are split into four peaks due to the electron and hole Zeeman splitting (figure 13(b)). A weak emission is observed at lower energy sides, in which the D_0X decays to higher orbital states such as 2s, 2p, ... of the D_0 state. These lines are called two-electron satellite (TES) emissions. The measured energy spectra for the transitions from the accepter bound excitons A_0X to the neutral acceptor A_0 with nth s-orbital states ($n = 1 - 5$) are plotted and compared with the hydrogenic model (solid line), $E_{A_0X} - E_{A_0} + \frac{1}{n^2}R_y^*$, in figure 14(b), where E_{AX}, E_{A_0} and R_y^* are the acceptor bound exciton energy, the ionization threshold energy and the binding energy of the neutral acceptor.

7.2. Spin relaxation time T_1 and decoherence time T_2 of electron spins

The spin relaxation time T_1 of the electron spin in an ensemble of Si:GaAs donor system was measured by first initializing the electron spin to its ground state by optical pumping, waiting for a variable delay time τ and sending a resonant optical probe pulse to detect the excited state population as shown in figure 15(a) [36]. A typical measurement result of the recovery trace to thermal equilibrium is shown in the inset of figure 15(b). From such a recovery trace, we can estimate the spin relaxation time T_1. Figure 15(b) shows the measured T_1 versus the dc magnetic field B_{ext}. T_1 increases with decreasing B_{ext} according to the law $B_{\text{ext}}^{-3.8\pm0.2}$ and saturates at $T_1 \simeq 4$ ms at $B_{\text{ext}} \leqslant 4T$. This saturation behavior is an experimental artifact due to the leakage of a blocked optical pumping beam during a supposedly free relaxation time period τ. The power

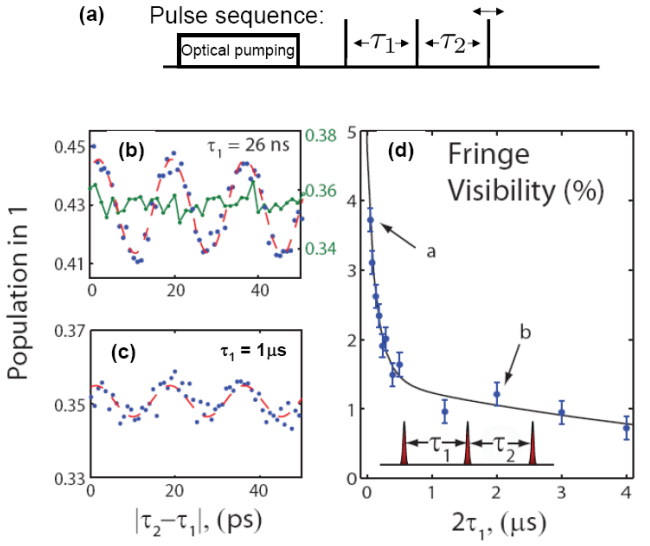

Figure 16. (a) A pulse sequence for Hahn's spin-echo setup. (b), (c) The Larmor precession signals for $2\tau_1 = 52$ ns and 2 μs. A green trace in (b) means there is no Larmor signal if there is no refocusing pulse. (d) The fringe visibility versus delay time $2\tau_1$ [38].

law of $T_1 \propto B_{\text{ext}}^{-4}$ agrees with the theoretical prediction based on spin–lattice relaxation model [37].

The dephasing time T_2^* of the electron spin in a Si:GaAs system is determined by the surrounding nuclear spin bath fluctuations and of the order of 1–10 ns. This was confirmed by the coherent population trapping experiment and also by the off-resonant stimulated Raman scattering experiment in our system [35].

We used three optical pulses, each of duration 2 ps, to construct a Hahn spin-echo setup to suppress the effect of nuclear spin bath inhomogeneity, as shown in figure 16(a) [38]. If there is no central (refocusing) pulse, there is no Larmor precession signal for the time interval $\tau_1 = 26$ ns $\gg T_2^*$ as shown in figure 16(b). However, if we inject the central (refocusing) pulse, the spin-echo signal is clearly observed for $2\tau_1 = 52$ ns and 2 μs as shown in figure 16(b) and (c). Figure 16(d) summarizes the optical pulse spin echo experiment, which suggests the spin-echo signal decays with an exponential time constant of $T_2 \simeq 6.7 \pm 2.5$ μs. The value is comparable to the inverse of the hyperfine coupling between the electron spin and nuclear spin in an Si:GaAs system. This means that a qubit of information could be transferred from the electron spin to the nuclear spin before the electron spin loses the quantum information.

The ratio of the decoherence time to single spin rotation time, $T_2/_{\text{pulse}}$, is of the order of $\sim 7 \times 10^6$. Recall, however, that an arbitrary one-qubit SU(2) operation requires one-half Larmor period of about 10 ps, so the ratio of decoherence time to the arbitrary one-qubit gate time is of the order of $\sim 7 \times 10^5$. However, the electron spins of Si:GaAs can be manipulated with a limited rotation angle by the current experiment with ~psec optical pulses [39].

7.3. Spin relaxation time and decoherence time of nuclear spins

The nuclear spin relaxation time T_1 and decoherence time T_2 of ^{29}Si nuclear spins were measured for a nuclear spin

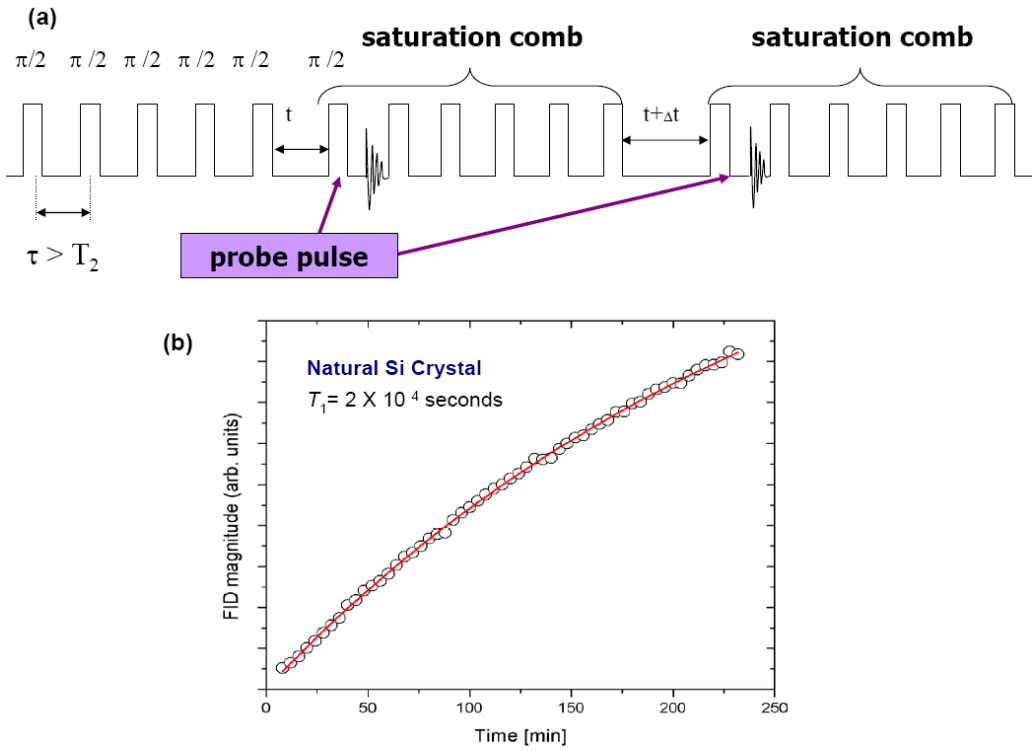

Figure 17. (a) An rf pulse sequence of saturation comb for measuring a T_1 time for ^{29}Si nuclear spins. (b) The FID signal versus delay time for a natural silicon crystal at 300 K [40].

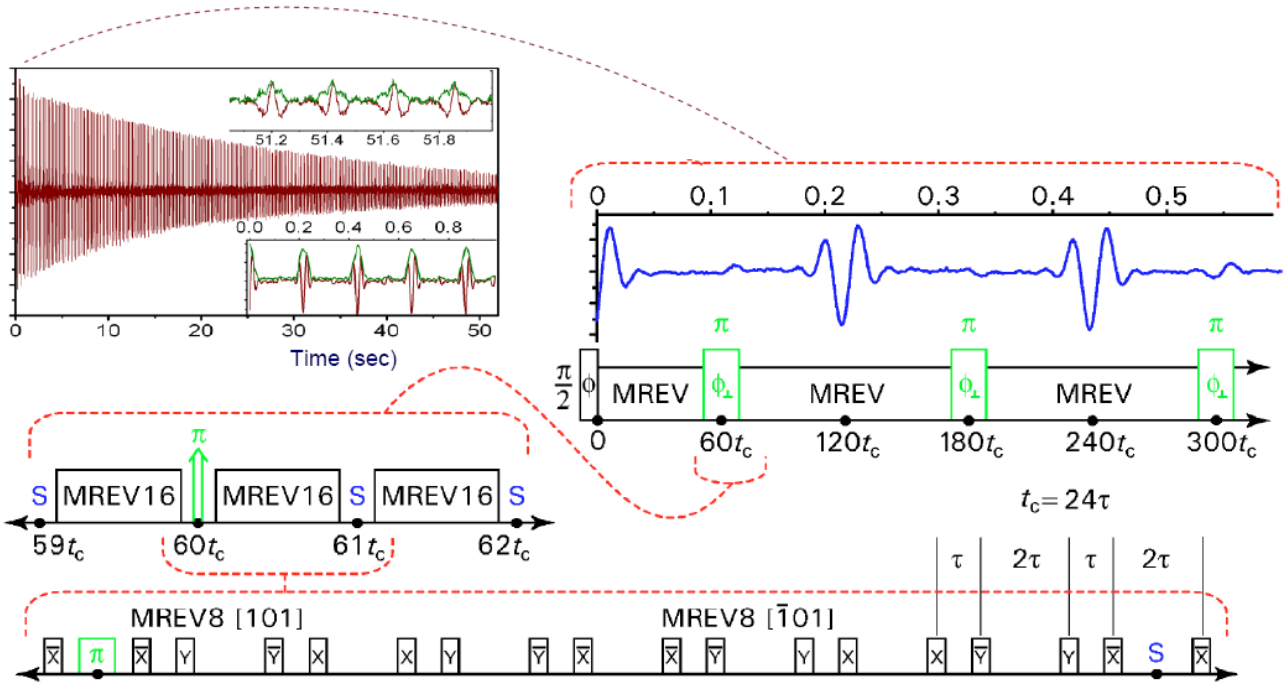

Figure 18. The spin-echo signal from ^{29}Si nuclear spins in a natural silicon crystal at 300 K. The CPMG π-pulse sequence and MREV-18 $\pi/2$ pulse sequence are concatenated to suppress the magnetic field fluctuation and iso-spin dipolar coupling [41].

ensemble in a single crystal of silicon. The T_1 time of ^{29}Si nuclear spins is measured by the saturation comb (multiple $\pi/2$ pulse sequence separated by a time interval much longer than T_2^*) which prepares the statistical mixture of equal populations in the ground and excited spin states in a relatively short time (figure 17(a)) [40]. The recovery of a thermal equilibrium population difference is monitored through free induction decay (FID) signals after the first $\pi/2$ pulse (probe pulse) of the saturation comb as shown in figure 17(b). For isotopically natural, single-crystal silicon, T_1 is extremely long at multiple hours at room temperature. But even for the more hostile environment of a ^{29}Si enriched sample, in which nuclear–nuclear dipolar coupling is strong, the T_1 time is longer than 2 h at 300 K and longer than 8 h at 10 K. In

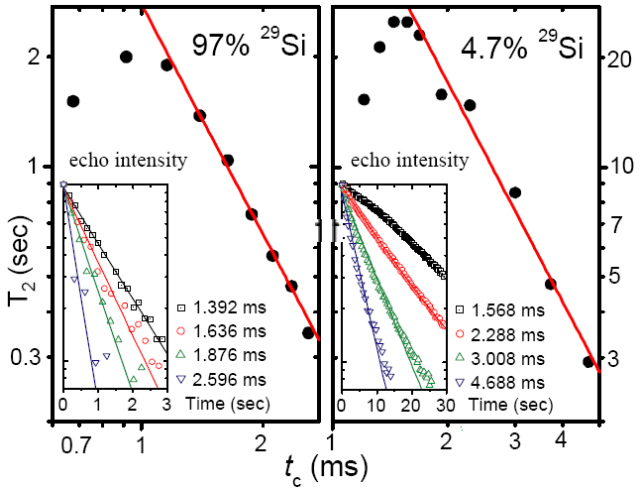

Figure 19. The inferred T_2 time of ^{29}Si nuclear spins versus the cycling time of the MREV-16 $\pi/2$ pulse sequence at 300 K [41].

general, spin-1/2 nuclei in semiconductor environments are very long lived.

The nuclear T_2 time is measured in an ensemble NMR experiment by combining the famous CPMG π-pulse sequence for refocusing the fluctuating magnetic field along the quantization axis and the MREV-16 $\pi/2$ pulse sequence for eliminating the dipolar coupling among iso-spins (^{29}Si–^{29}Si), as shown in figure 18 [41]. The inferred T_2 time in this measurement for a natural silicon and ^{29}Si enriched sample are shown as a function of rf pulse cycle time t_c in figure 19 [41]. The quadratic dependence of T_2 on t_c, $T_2 \propto 1/t_c^2$, agrees with average Hamiltonian theory for the MREV decoupling pulse sequence. The T_2 time is ~2 s for a ^{29}Si enriched sample and ~25 s for a natural silicon crystal even at 300 K. Those numbers are long enough even for ultra long distance quantum repeater system applications.

8. Generation and characterization of indistinguishable single photons

8.1. Generation of single photons and quantum interference

In order to implement the second scheme of entanglement distribution based on a single photon bus, a QD must emit a single photon at a time. Generation of single photons from a patterned QW [42], self-assembled QD [43–45] and position controlled QD [46] have been demonstrated. However, for a quantum repeater application, spontaneously emitted single photons should be Fourier transform limited and should exhibit negligible timing jitter. This has been demonstrated for sequentially generated single photons from an InGaAs QD embedded in a post-microcavity [47]. In this system, the spontaneous emission lifetime is short compared with the decoherence time of the excitonic dipole of ~1 ns, and so it expected that the single photon pulse should be Fourier-transform limited. The timing jitter of single-photon emission from a QD is determined by the energy relaxation time of ~10 ps from the 2e–2h optical excitation level to the 1e–1h emission level. If the single photon pulse duration (determined by the spontaneous emission lifetime) is much longer than ~10 ps, the timing jitter can be neglected.

Table 1. The two-photon correlation function $g^{(2)}(0)$, the ratio g of the probability of emitting two photons in either one of the two consecutive pulses to the probability of emitting one photon in each pulse, the spontaneous emission lifetime τ_s, the first-order coherence time τ_c, $1/e$ width of the HOM dip τ_m and the two photon overlap at zero path-length difference $V(0)$ of the three devices [47].

	$g^{(2)}$	g	τ_s(ps)	τ_c(ps)	τ_m(ps)	$V(0)$
Dot1	0.053	0.039	89	48	80	0.72
Dot2	0.067	0.027	166	223	187	0.81
Dot3	0.071	0.025	351	105	378	0.74

The three GaAs/AlAs micropost DBR microcavities with a single InGaAs QD are fabricated to realize an appropriate cavity-enhanced spontaneous emission rate. The performance of these three devices are summarized in table 1. The second-order correlation function $g^{(2)}(0)$ is less than 0.1, which confirms a single QD emitter exists inside a cavity. The spontaneous emission lifetime is $\tau_s = 90$–350 ps, which satisfies $\tau_s \ll 1$ ns and $\tau_s \gg 10$ ps. The indistinguishability was tested by the Hong–Ou–Mandel (HOM) interferometry shown in figure 20(a). Five peaks appear within the central cluster, corresponding to three types of coincidence events. For peaks 1 and 5 at $\tau = \pm 4$ ns, the first photon follows the short arm of the interferometer and the second photon follows the long arm. For peaks 2 and 4 at $\tau = \pm 2$ ns, both photons follow the same arm. For peak 3 at $\tau = 0$, the first photon follows the long arm and the second photon follows the short arm such that the two photons collide at the beam splitter. The reduction of the coincident count rate (peak intensity 3 compared with 2 and 4 in figure 20(b)) reveals the quantum interference between indistinguishable photons. From the numerical fit to the HOM dip as shown in figure 20(c), the overlap of the quantum wavefunctions of two single photons can be estimated to be 0.7–0.8 and the results are summarized in table 1. For all three devices, we observe reductions in the coincidence probability near $\Delta t = 0$ by factors of 0.61, 0.69 and 0.62 for QDs 1, 2 and 3, respectively. The remaining coincidences are partly due to optical imperfections in the setup such as beam splitter's reflection to transmission ratio $R/T = 1.1$ and the interference fringe contrast $(1-\varepsilon) = 0.92$ measured when an ideal monochromatic laser source is sent into the interferometer, and accounts for optical surface imperfections. Without these imperfections, the coincidence reduction factors would be $V(0) = 0.72$, 0.81 and 0.74, respectively.

8.2. Violation of Bell's inequality

The quality of generated indistinguishable single photons can be studied through the test of violation of Bell's inequality. The experimental system is shown in figure 21(a) [48], where the two single photons in the same horizontal linear polarization, $|H\rangle_1|H\rangle_2$, is converted to a polarization entangled state, $\frac{1}{\sqrt{2}}(|H\rangle_1|V\rangle_2 - |V\rangle_1|H\rangle_2)$, via linear optical circuits and post-selection of coincidence counts at D_A and D_B. The two photon polarization state is reconstructed by state tomography as shown in figure 21(b). The density matrix of the two polarization states in the $|HH\rangle$, $|HV\rangle$, $|VH\rangle$ and

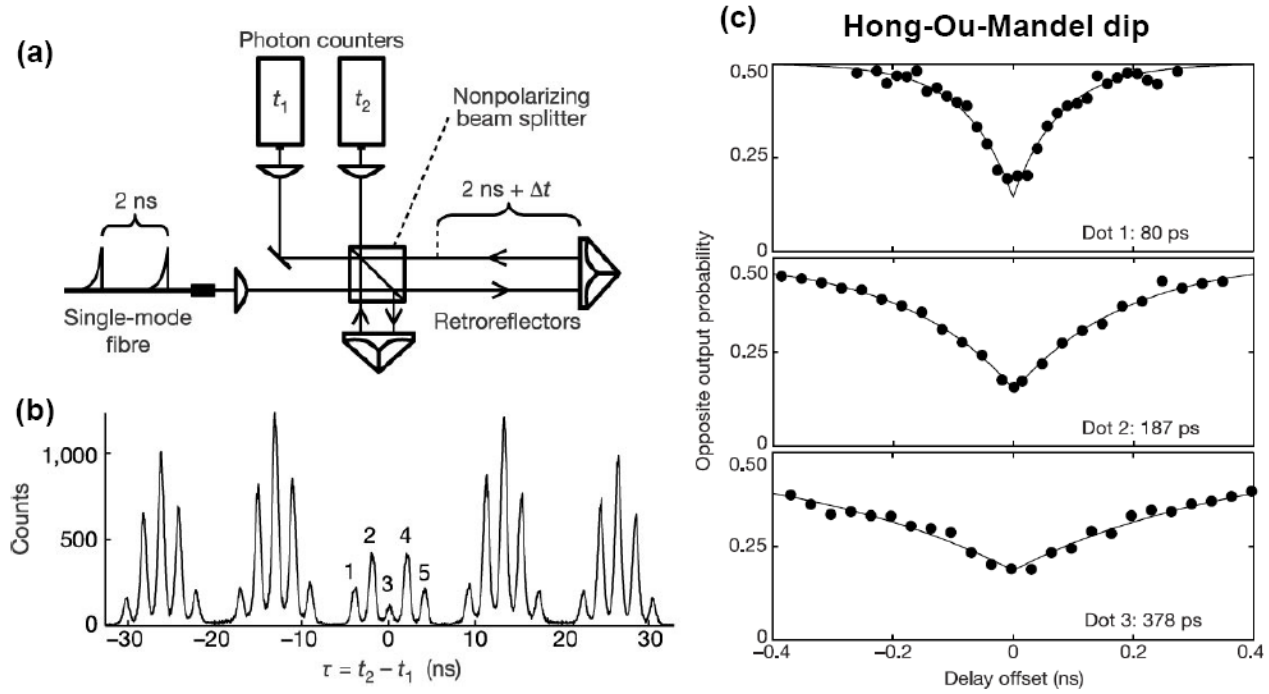

Figure 20. (A) A Michelson-type interferometer for colliding two photons separated by 2 ns. (b) Coincidence count rate as a function of a relative delay time between a photon detection at one counter (t_1) and the other (t_2). (c) Coincidence count rate $g^{(2)}(\tau)$ versus delay offset for the three devices [47].

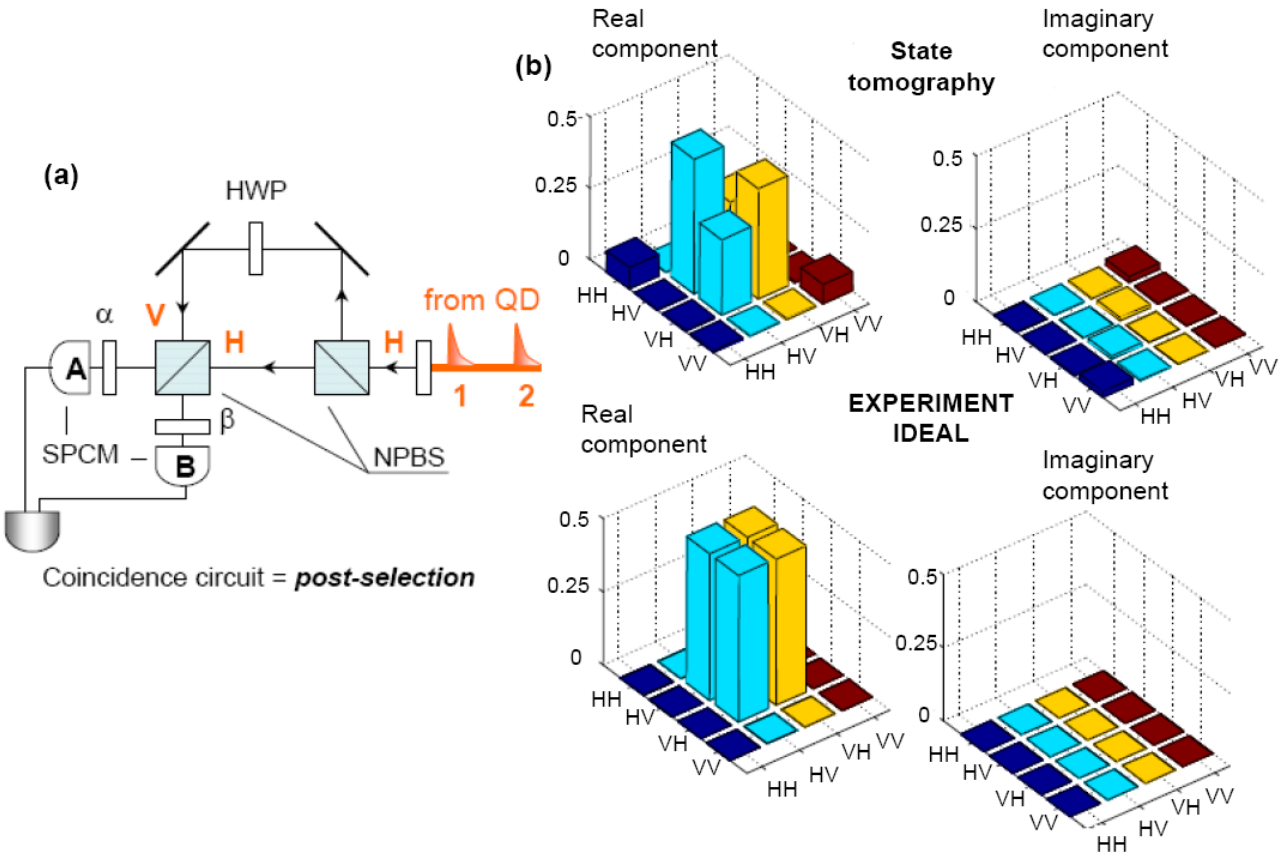

Figure 21. (a) Experimental setup for the entanglement formation and the test of violation of Bell's inequality. (b) Reconstructed polarization density matrix and maximally entangled-state density matrix [48].

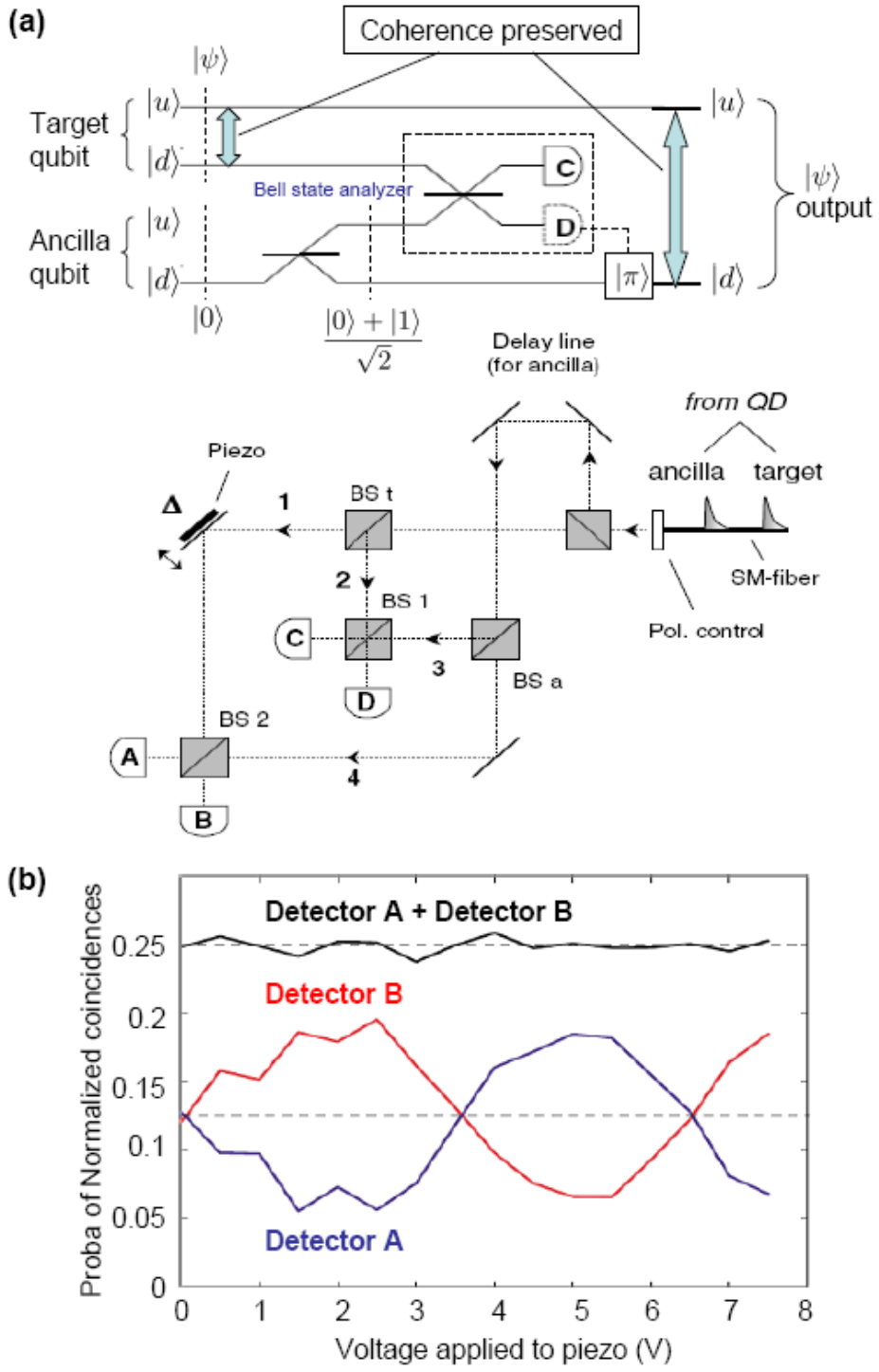

Figure 22. (a) Experimented setup for single-mode quantum teleportation of a target photon. (b) Verification of single-mode teleportation [51].

$|VV\rangle$ basis is given by

$$\hat{\rho} = \frac{1}{\frac{R}{T} + \frac{T}{R} + 4g^{(2)}} \begin{pmatrix} 2g^{(2)} & & & \\ & R/T & -V & \\ & -V & T/R & \\ & & & 2g^{(2)} \end{pmatrix}, \quad (3)$$

where R and T are the reflection and transmission coefficients of the second NPBS in figure 21(a), $g^{(2)}$ is the second-order correlation function and V is the overlap between two single photon wave functions. Using the values for R/T, $g^{(2)}$ and V measured independently, we obtain an excellent quantitative agreement of our model to the experimentally determined density matrix, with a fidelity of $F = \mathrm{Tr}[\hat{\rho}_{\mathrm{exp}}^{1/2}\hat{\rho}_{\mathrm{model}}\hat{\rho}_{\mathrm{exp}}^{1/2}]$ as high as 0.994 [48]. Using the Peres criterion [49], the negativity is ∼0.43, which indicates the created state is entangled, i.e. non-separable.

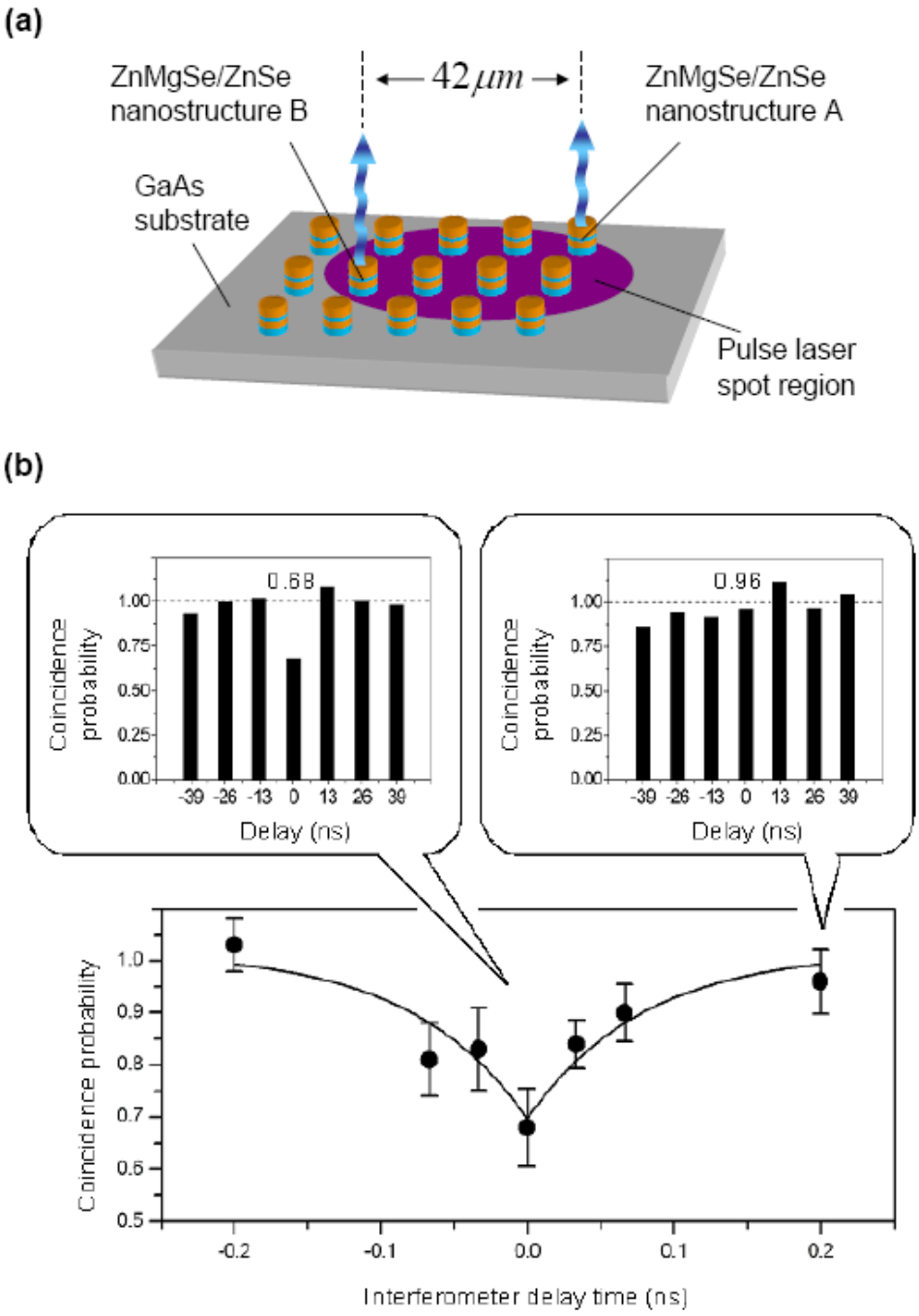

Figure 23. (a) Experimental system for generation of indistinguishable single photons from two ^{19}F:ZnSe donor impurities. (b) The observed HOM dip [52].

Following [50], if we define the correlation function $E(\alpha, \beta)$ for analyzer setting α and β as

$$E(\alpha, \beta) = \frac{C(\alpha, \beta) + C(\alpha^{\perp}, \beta^{\perp}) - C(\alpha^{\perp}, \beta) - C(\alpha, \beta^{\perp})}{C(\alpha, \beta) + C(\alpha^{\perp}, \beta^{\perp}) + C(\alpha^{\perp}, \beta) + C(\alpha, \beta^{\perp})}, \quad (4)$$

the local realistic assumptions lead to the inequality

$$S = |E(\alpha, \beta) - E(\alpha', \beta)| + |E(\alpha', \beta) + E(\alpha', \beta')| \leqslant 2, \quad (5)$$

that can be violated by quantum mechanics. Sixteen measurements were performed for all combinations of polarizer settings among $\alpha \in \{0^{\circ}, 45^{\circ}, 90^{\circ}, 135^{\circ}\}$ and $\beta \in \{22.5^{\circ}, 67.5^{\circ}, 112.5^{\circ}, 157.5^{\circ}\}$, which produced the experimental result $S \sim 2.38 \pm 0.18$. Thus, the CHSH inequality was violated by two standard deviations.

8.3. Quantum teleportation

The quality of generated indistinguishable single photons can be further tested by constructing a single-mode quantum teleportation gate [51]. An experimental setup is shown in figure 22(a), where the two single photons are used as a dual-rail target qubit and ancilla qubit and the linear optics Bell state measurement is employed. The mode $|d\rangle$ of the target qubit is teleported to the mode $|d\rangle$ of the ancilla qubit, which was confirmed by the interference pattern for

the mixing output of the mode $|u\rangle$ of the target qubit and the mode $|d\rangle$ of the ancilla qubit, as shown in figure 22(b). The finite contrast in figure 22(b) is mainly due to a residual distinguishability between ancilla and target photons, which is parameterized by V. Slight misalignments and imperfections in optics also result in an imperfect mode matching at BS1 and BS2, reducing the first-order interference visibilities V_1 and V_2. Finally, the residual presence of two-photons ($g^{(2)} > 0$) can reduce the contrast. These parameters can be independently measured as $V \sim 0.75$, $V_1 \sim 0.92$, $V_2 \sim 0.91$ and $g^{(2)} \sim 0.02$. The contrast C in counts at detector A or B should be $C_{\text{model}} = VV_1V_2/(1+g^{(2)}/2) \sim 0.62$. This predicted value compares well with the observed value of $C_{\text{exp}} \sim 0.60$. The fidelity of teleportation is $F = (1+C)/2 \sim 0.8$ in this experiment [51].

8.4. Indistinguishable single photon generation from two quantum memories

In order to distribute an entangled state in two remote quantum memories, the indistinguishable single photons must be generated simultaneously from two independent quantum memories. This function has been demonstrated recently using two ^{19}F:ZnSe donor impurities [52]. The experimental system is shown in figure 23(a), in which two post-structure devices with a single ^{19}F donor impurity simultaneously emit single photons. The measured $g^{(2)}(0)$ for these two devices are ∼0.25 and ∼0.40, respectively. The observed HOM dip is shown in figure 23(b). The visibility and the quantum mechanical overlap of the two single photon wavefunction are ∼31% and ∼65 ± 13%, respectively.

9. Conclusions

The ingredients we have discussed show strong promise for scalable quantum information processing, but we must not forget the challenges in designing large-scale systems. In a large-scale quantum computer or quantum repeater, the cost of communication will dominate the performance and resource requirements. The presence of realistic optical losses in communication channels and optical cavities will place severe demands on the architectural design of quantum processors, as will finite yields of qubits and finite chip-sizes. As an example, for a nested-purification-based [7, 8] quantum repeater system implemented with semiconductor cavity QED and optical fiber over a communication distance of 10 000 km, ∼1000 repeater nodes, $\sim 4 \times 10^3$ quantum memories (qubits) per node and gate errors less than 0.5% are required to create one EPR-Bell state every ∼100 ms [18]. As another example, for a purification-based semiconductor cavity QED one-way (cluster state) quantum computer with topological quantum error correction [9, 10] with a finite-device-yield system, factoring a 2048-bit number by Shor's algorithm may require resources on the order of $\sim 10^4$ logical qubits, $\sim 10^9$ physical qubits (lattice size), gate errors smaller than ∼0.2%, and decoherence times exceeding ∼50 ms [53]. Starting with a physical qubit operation clock rate of 10 GHz in this model architecture, the final execution time is still of the order of a year [53]. The added overhead for error correction makes quantum information processing systems very expensive, and emphasizes the need for fast operation times and efficient qubit-to-qubit communication.

Here, we have presented a candidate physical system for these emerging technologies: optically controlled QDs. This system may cope with the daunting demands of fast initialization, coherent manipulation, mutual couplings and rapid measurements, all using bright laser pulses and a simple planar microcavity. The lattice size (number of physical qubits) can scale up to $\sim 10^9$ in this system, so a single chip or multiprocessors with of the order of ten chips can accommodate the above design criteria. Intrachip and interchip entanglement distributions can be achieved either by the phase shift measurement of coherent state probe pulses or the generation and coincidence detection of indistinguishable single photons. Suppression of decoherence for electron spin processors by an optical refocusing pulse sequence has been successfully demonstrated and the T_2 time seems to be long enough to allow transfer of a qubit of information to a nuclear spin memory with a T_2 time much longer than ∼1 s. Our results suggest that such optical semiconductor technology has the potential to scale to a system capable of attacking classically intractable communication and computation problems.

Acknowledgments

This work was partially supported by NTT, JST/SORST, Special Coordination Funds for Promoting Science and Technology, MEXT and MURI.

References

[1] Deutsch D 1985 *Proc. R. Soc. London* A **400** 97
[2] Feynman R P 1982 *Int. J. Theor. Phys.* **21** 467
[3] Yamamoto Y, Kitagawa M and Igeta K 1988 *Proc. 3rd Asia Pacific Physics Conf.* (Singapore: World Scientific) p 779
[4] Imoto N, Haus H A and Yamamoto Y 1985 *Phys. Rev.* A **32** 2287
[5] Yamamoto Y, Machida S, Igeta K and Horikoshi Y 1989 *Conf. and Quantum Optics VI* ed J H Eberly *et al* (New York: Plenum) p 1249
[6] Björk G, Machida S, Yamamoto Y and Igeta K 1991 *Phys. Rev.* A **44** 669
[7] Briegel H J, Dür W, Cirac J I and Zoller P 1998 *Phys. Rev. Lett.* **81** 5932
[8] Dür W, Briegel H J, Cirac J I and Zoller P 1999 *Phys. Rev.* A **59** 169
[9] Raussendorf R, Harrington J and Goyal K 2007 *New J. Phys.* **9** 199
[10] Raussendorf R and Harrington J 2007 *Phys. Rev. Lett.* **98** 190504
[11] Allen L and Eberly J H 1975 *Optical Resonance and Two-Level Atoms* (New York: Wiley)
[12] Björk G, Pau S, Jacobson J and Yamamoto Y 1994 *Phys. Rev.* B **50** 17336
[13] Bonadeo N H, Chen G, Gammon D and Steel D 2000 *Phys. Status Solidi* **221** 5
[14] Guest J R *et al* 2002 *Phys. Rev.* B **65** 241310
[15] Hours J, Senellart P, Peter E, Cavanna A and Bloch J 2005 *Phys. Rev.* B **71** 161306
[16] Schneider C, Strau M, Sünner T, Huggenberger A, Wiener D, Reitzenstein S, Kamp M, Höfling S and Forchel A 2008 *Appl. Phys. Lett.* **92** 183101
[17] van Loock P, Ladd T D, Sanaka K, Yamaguchi F, Nemoto K, Munro W J and Yamamoto Y 2006 *Phys. Rev. Lett.* **96** 240501
[18] Ladd T D, van Loock P, Nemoto K, Munro W J and Yamamoto Y 2006 *New J. Phys.* **8** 184

[19] Ward M B, Karimov O Z, Unitt D C, Yuan Z L, See P, Devaud D G, Shield A, Atkinson P and Ritche D A 2005 *Appl. Phys. Rev.* **86** 201111
[20] Bayer M and Forchel A 2002 *Phys. Rev.* B **65** 195305
[21] Press D, Ladd T D, Zhang B and Yamamoto Y 2008 *Nature* **456** 218
[22] Press D, Götzinger S, Reitzenstein S, Hofmann C, Löffler A, Kamp M, Forchel A and Yamamoto Y 2007 *Phys. Rev. Lett.* **98** 117402
[23] Yamamoto Y, Machida S, Igeta K and Björk G 1991 Controlled spontaneous emission in microcavity semiconductor lasers *Coherence, Amplification and Quantum Effects in Semiconductor Lasers* ed Y Yamamoto (New York: Wiley)
[24] Jiang S, Machida S, Takiguchi Y and Yamamoto Y 1998 *Appl. Phys. Rev.* **73** 3031
[25] Clark S M, Fu K-M, Ladd T D and Yamamoto Y 2007 *Phys. Rev. Lett.* **99** 040501
[26] Berezovsky J, Mikkelson M H, Stolts N G, Coldren L A and Awschalom D D 2008 *Science* **320** 349
[27] Imamoglu A, Awschalom D D, Burkard G, DiVincenzo D P, Loss D, Sherwin M and Small A 1999 *Phys. Rev. Lett.* **83** 4204
[28] Spiller T P, Nemoto K, Braunstein S L, Munro W J, van Loock P and Milburn G 2006 *New J. Phys.* **8** 30
[29] Ladd T D and Yamamoto Y in preparation
[30] Feng X-L, Zhang Z-M, Li X-D, Gong S-Q and Xu Z-Z 2003 *Phys. Rev. Lett.* **90** 217902
[31] Duan L-M and Kimble H J 2003 *Phys. Rev. Lett.* **90** 253601
[32] Simon C and Irvine W T M 2003 *Phys. Rev. Lett.* **91** 110405
[33] Moehring D L, Maunz P, Olmschenk S, Younge K C, Matsukevich D N, Duan L M and Monroe C 2007 *Nature* **449** 68
[34] Karasyuk V A, Beckett D G S, Nissen M K, Villemaire A, Steiner T W and Thewalt M L W 1994 *Phys. Rev.* B **49** 16381
[35] Fu K M, Santori C, Stanley C, Holland M C and Yamamoto Y 2005 *Phys. Rev. Lett.* **95** 187405
[36] Fu K M, Yeo W, Clark S, Santori C, Stanley C, Holland M C and Yamamoto Y 2006 *Phys. Rev.* B **74** 121304
[37] Woods L M, Reinecke T L and Lyanda-Geller Y 2002 *Phys. Rev.* B **66** 161318
[38] Clark S, Fu K M, Zhang Q, Ladd T D, Stanley C and Yamamoto Y 2009 *Phys. Rev. Lett.* **102** 247601
[39] Fu K M, Clark S, Santori C, Stanley C R, holland M C and Yamamoto Y 2008 *Nat. Phys.* **4** 780
[40] Verhulst A S, Maryenko D, Yamamoto Y and Ito K M 2003 *Phys. Rev.* B **68** 054105
[41] Ladd T D, Maryenko D, Yamamoto Y, Abe E and Ito K M 2005 *Phys. Rev.* B **71** 014401
[42] Kim J, Benson O, Kan H and Yamamoto Y 1999 *Nature* **397** 500
[43] Michler P, Kiraz A, Becher C, Schoenfeld W V, Petroff P M, Zhang L, Hu E and Imamoglu A 2000 *Nature* **290** 2282
[44] Santori C, Pelton M, Solomon G, Dale Y and Yamamoto Y 2001 *Phys. Rev. Lett.* **86** 1502
[45] Yuan Z, Kardynal B E, Stevenson R M, Shields A J, Lobo C J, Cooper K, Beattie N S, Ritchie D A and Pepper M 2002 *Science* **295** 102
[46] Schneider C, Heindel T, Huggenberger A, Weinmann P, Kistner C, Kamp M, Reitzenstein S, Höfling S and Forchel A 2009 *Appl. Phys. Lett.* **94** 111111
[47] Santori C, Fattal D, Vuckvic J, Solomon G and Yamamoto Y 2002 *Nature* **419** 594
[48] Fattal D, Inoue K, Vuckvic J, Santori C, Solomon G and Yamamoto Y 2004 *Phys. Rev. Lett.* **92** 037903
[49] Peres A 1996 *Phys. Rev. Lett.* **77** 1413
[50] Clauser J, Horne M, Shimony A and Holf R 1969 *Phys. Rev. Lett.* **23** 880
[51] Fattal D, Diamanti E, Inoue K and Yamamoto Y 2004 *Phys. Rev. Lett.* **92** 037904
[52] Sanaka K, Pawlis A, Ladd T D, Lischka K and Yamamoto Y 2009 *Phys. Rev. Lett.* to be published
[53] Van Meter R, Ladd T D, Fowler A G and Yamamoto Y 2009 arXiv:quant-ph/0906